Coherence and dimensionality of intense spatio-spectral twin beams

Jan Peřina Jr.

RCPTM, Joint Laboratory of Optics of Palacký University and Institute of
Physics of Academy of Sciences of the Czech Republic, Faculty of Science,
Palacký University, 17. listopadu 12, 771 46 Olomouc, Czech Republic

Spatio-spectral properties of twin beams at their transition from low to high intensities are analyzed in parametric and paraxial approximations using the decomposition into paired spatial and spectral modes. Intensity auto- and cross-correlation functions are determined and compared in the spectral and temporal domains as well as the transverse wave-vector and crystal output planes. Whereas the spectral, temporal and transverse wave-vector coherence increases with the increasing pump intensity, coherence in the crystal output plane is practically independent on the pump intensity owing to the mode structure in this plane. The corresponding auto- and cross-correlation functions approach each other for larger pump intensities. Entanglement dimensionality of a twin beam is determined comparing several approaches.

I. INTRODUCTION

The nonlinear process of parametric down-conversion [1] is the most frequently used process for the generation of light with nonclassical properties. It provides entangled photon pairs in its spontaneous regime [2]. Photons comprising a photon pair can be entangled in different degrees of freedom including polarization, frequency, emission direction or orbital angular momentum. Entanglement in all these degrees of freedom has been found useful both for testing the rules of quantum mechanics [3] and applications [4].

On the other hand, parametric down-conversion generates the so-called twin beams when stimulated emission is important. Such twin beams are composed of a signal and an idler fields with large intensities that are mutually strongly correlated. These correlations occur both in the spectra and emission directions as a consequence of the properties that give different kinds of entanglement at single-photon level. Moreover, the intensity correlations are so strong that they violate the standard shot-noise limit (sub-shot-noise correlations) [5, 6]. This nonclassical property originates in the genuine pairwise character of parametric down-conversion at its quantum level. An experimental evidence of sub-shot-noise intensity correlations has been given in [7–10]. Such states are useful also for quantum imaging. Even imaging based upon sub-shot-noise intensity correlations has been recently demonstrated [11, 12].

Spontaneous parametric down-conversion with its production of entangled photon pairs has been studied by far the most frequently. In theory, the first-order solution of the appropriate Schrödinger equation provides a two-photon amplitude that determines all properties of entangled photon pairs [13, 14]. This simple formalism is also easily applicable to more complex nonlinear structures generating photon pairs (waveguides, fibers, layered structures, Bragg-reflector waveguides, periodically-poled structures, for details, see, e.g., [15]). At present, photon pairs with more-less arbitrary properties can be efficiently generated due to many kinds of available sources.

On the other hand, investigations of twin beams have been concentrated to more intense twin beams [16] because of the lack of detection techniques capable to detect intensities at the transition from the single-photon level to the intense ('classical') one [17]. This has required intense pump lasers that have provided quasi-monochromatic beams (usually picosecond pulses). As a consequence, the developed theoretical models usually invoke the quasi-monochromatic approximation. When combined with the pump-field quasi-plane-wave approximation, a twin beam in the model has been decomposed into many more-less independent pairs of signal and idler modes localized both in the spectrum and transverse wave-vector plane [18–21]. The dynamics of individual pairs of modes has then been treated by the solution of linear Heisenberg equations. Under more general conditions, numerical solution of the Maxwell equations using a statistical ensemble of initial conditions has occurred useful [22].

The Schmidt decomposition [23, 24] of two-photon amplitudes introduced for pure states at single-photon level has become popular in the last couple of years due to its ability to quantify entanglement in larger Hilbert spaces and to reveal the genuine dual structure of a bipartite entangled state [25, 26]. Such modes can even be selected from a beam [27–30] or changed on demand. However, the revealed paired modes have been found suitable also for making the bridge between the perturbation theory of weak paired fields and that of the intense beams. The corresponding theory has been based upon the solution of Heisenberg equations for individual and independent paired modes, similarly as the theory developed earlier for intense twin beams. Contrary to this theory based on localized modes, it uses the Schmidt modes spread over the whole spectrum or transverse wave-vector plane [31]. This makes the theory suitable for describing coherence of the twin beams and especially its growth with the increasing pump intensity. It has already been applied to

describe spectral properties and amplitude squeezing of weaker as well as more intense twin beams [32–34]. Also angular properties of the twin beams have been addressed [35]. Even nonlinear waveguides with back-scattering have been investigated using this approach [36].

However, the spectral and spatial properties of a twin beam have only been considered separately in this approach up to now. This represents a serious simplification as the spectral and spatial modes are inevitably mutually coupled in the nonlinear interaction. The consideration of only the spectral (or spatial) modes allows to understand the behavior of twin beams only to certain extent as the approach is not able to describe correctly a common dynamics of both spectral and spatial degrees of freedom. The 'one-dimensional Schmidt-mode models' developed up to now are in fact simple 'fenomenological' models that are conveniently applied for interpreting the experimental results obtained under specific conditions [strong spatial (spectral) filtering for the spectral (radial transverse direction) model]. On the other hand, real down-conversion occurs in a nonlinear crystal with all possible spatio-spectral modes participating in the interaction. As bulk nonlinear crystals are commonly used for the generation of intense twin beams, the number of participating modes is large. Moreover, the number of modes giving an important (intensity) contribution to the generated twin beam is also large. That is why, a general spatio-spectral model of twin-beam generation is necessary.

In this contribution, we develop the Schmidt-mode approach for describing such a general spatio-spectral twin beam. Using the paired spatio-spectral modes, we address coherence of the twin beams determining their auto- and cross-correlation functions in the spectral and temporal domains, transverse wave-vector plane, and crystal output plane. Properties of the twin beams manifested under different experimental conditions are compared. Special attention is paid to the dependence of coherence on the pump intensity. Coherence properties of the twin beams together with their photon-number statistics are used to compare several suitable quantifiers of their dimensionality [37, 38]. This provides a complete picture of an intense spatio-spectral twin beam.

The developed model can easily be generalized to more complex nonlinear structures with nonlinearity homogeneous in the transverse plane including poled nonlinear crystals [39, 40] and nonlinear layered structures [15]. It can even be applied for the description of intense twin beams originating in the nonlinear process of four-wave mixing, both in nonlinear crystals with $\chi^{(3)}$ nonlinearity and atomic ensembles. The four-wave mixing in atomic ensembles [41], though being partly noisy [42], is very attractive due to the high effective nonlinear coupling constants. Noiseless spatially-resolved amplification [43] as well as entangled images [12] in this scheme using ^{85}Rb vapors have been experimentally demonstrated.

Recently, the first experimental investigations of ultra-intense twin beams have been reported both for multi-mode [17, 44–48] as well as single-mode (bright squeezed-vacuum states) fields [49]. The effects of pump-field depletion have been observed. Also back-flow of energy from the twin beam into the pump field may occur. These processes affect spectra as well as transverse profiles of the twin beams [45–47]. Here, we restrict our attention to the case of un-depleted pump fields (parametric approximation). However and importantly, the generalization of the theory to account for pump-field depletion and back-flow of energy is possible due to the fact that the model incorporates all spatio-spectral degrees of freedom. This generalization will be reported elsewhere.

The paper is organized as follows. A spatio-spectral model of parametric down-conversion based upon the Schmidt paired modes is developed in Sec. II. Quantities characterizing spectral and temporal properties of twin beams are defined in Sec. III. Several suitable quantifiers of dimensionality of a twin beam are introduced in Sec. IV. Spectral and temporal properties of twin beams as functions of the pump intensity are discussed in Sec. V. Properties of twin beams in the transverse wave-vector plane and the crystal output plane are analyzed in Sec. VI. Conclusions are drawn in Sec. VII. In Appendix A, twin beams are described in their transverse wave-vector plane (far field) and the crystal output plane (near field).

II. THEORY OF A SPATIO-SPECTRAL TWIN BEAM

Optical parametric down-conversion and its evolution along a nonlinear medium characterized by tensor d of second-order nonlinear coefficients is described by the momentum operator $\hat{G}_{\text{int}}$ written in the interaction representation as follows [50, 51]:

$$\hat{G}_{\text{int}}(z) = 4\epsilon_0 \int dx dy \int_{-\infty}^{\infty} dt$$
$$\left[d : E_{\text{p}}^{(+)}(\mathbf{r},t)\hat{E}_{\text{s}}^{(-)}(\mathbf{r},t)\hat{E}_{\text{i}}^{(-)}(\mathbf{r},t) + \text{H.c.} \right]; (1)$$

$\mathbf{r} = (x, y, z)$. In Eq. (1), $E_{\text{p}}^{(+)}$ describes the positive-frequency part of a classical pump electric-field amplitude and $\hat{E}_{\text{s}}^{(-)}$ $[\hat{E}_{\text{i}}^{(-)}]$ stands for the negative-frequency part of a signal- [idler-] field operator amplitude. Symbol : is shorthand for tensor shortening with respect to its three indices, ϵ_0 is permittivity of vacuum and H.c. replaces the Hermitian conjugated term.

The electric-field amplitudes $E_a^{(+)}(\mathbf{r},t)$ $[E_a^{(+)}(\mathbf{r},t) = E_a^{(-)*}(\mathbf{r},t)]$ of the interacting fields can be decomposed into harmonic plane waves with wave vectors $\mathbf{k}_a$ and frequencies ω_a:

$$E_a^{(+)}(\mathbf{r},t) = \frac{1}{\sqrt{2\pi}^3} \int d\mathbf{k}_a \, E_a^{(+)}(\mathbf{k}_a) \exp(i\mathbf{k}_a\mathbf{r} - i\omega_a t),$$
$$a = \text{p}, \text{s}, \text{i}. \tag{2}$$

We assume that the interacting fields can be described in paraxial approximation which provides the relation $\mathbf{k} = (k_x, k_y, k_z) = (k_x, k_y, k - [k_x^2 + k_y^2]/2k)$, $k = \sqrt{k_x^2 + k_y^2 + k_z^2}$, valid for fields propagating close to the z direction.

We consider a strong pump field with the Gaussian spectrum and Gaussian transverse profile. It is described in paraxial approximation as follows:

$$E_p^{(+)}(\mathbf{r}, t) = \frac{1}{\sqrt{2\pi}^3} \int d\mathbf{k}_p^\perp \int_0^\infty d\omega_p \, E_p^\perp(\mathbf{k}_p^\perp) E_p^\parallel(\omega_p)$$
$$\times \exp(ik_{p,x}x) \exp(ik_{p,y}y) \exp(ik_p z)$$
$$\times \exp\left(-i\frac{k_{p,x}^2 + k_{p,y}^2}{2k_p}z\right) \exp(-i\omega_p t); \quad (3)$$

$\mathbf{k}_p^\perp \equiv (k_{p,x}, k_{p,y})$ and $k_p = k_p(\omega_p)$. Temporal spectrum $E_p^\parallel(\omega_p)$ of the Gaussian pump pulse is expressed as:

$$E_p^\parallel(\omega_p) = \xi_p \sqrt{\frac{\tau_p}{\sqrt{2\pi}}} \exp\left[-\frac{\tau_p^2(\omega_p - \omega_p^0)^2}{4}\right]. \quad (4)$$

According to Eq. (4), the pump pulse has amplitude ξ_p, duration τ_p and carrying frequency ω_p^0. Provided that the pulsed pump field source has power P_p and repetition rate f, amplitude ξ_p is given by the relation

$$\xi_p = \sqrt{\frac{P_p \omega_p}{\epsilon_0 c^2 k_p f}}, \quad (5)$$

where c is the speed of light in vacuum. The pump field radially symmetric in its transverse plane is characterized by the Gaussian spatial spectrum

$$E_p^\perp(\mathbf{k}_p^\perp) = \frac{w_p}{\sqrt{2\pi}} \exp\left[-\frac{w_p^2(k_{p,x}^2 + k_{p,y}^2)}{4}\right], \quad (6)$$

where w_p gives the beam radius.

The signal and idler electric-field operator amplitudes $\hat{E}_s^{(-)}$ and $\hat{E}_i^{(-)}$ are decomposed similarly as the pump field in paraxial approximation:

$$\hat{E}_a^{(-)}(\mathbf{r}, t) = \frac{1}{\sqrt{2\pi}^3} \int d\mathbf{k}_a^\perp \int_0^\infty d\omega_a \, \hat{E}_a^{(-)}(\mathbf{k}_a^\perp, \omega_a)$$
$$\times \exp(-ik_{a,x}x) \exp(-ik_{a,y}y) \exp(-ik_a z)$$
$$\times \exp\left(i\frac{k_{a,x}^2 + k_{a,y}^2}{2k_a}z\right) \exp(i\omega_a t), \quad a = s, i. \quad (7)$$

The spectral operator amplitudes $\hat{E}_a^{(-)}(\mathbf{k}_a^\perp, \omega_a)$ can be expressed using creation operators $\hat{a}^\dagger(\mathbf{k}_a^\perp, \omega_a)$ that add a photon into the mode with transverse wave vector $\mathbf{k}_a^\perp$ and frequency ω_a:

$$\hat{E}_a^{(-)}(\mathbf{k}_a^\perp, \omega_a) = -i\sqrt{\frac{\hbar\omega_a^2}{2\epsilon_0 c^2 k_a}} \, \hat{a}_a^\dagger(\mathbf{k}_a^\perp, \omega_a); \quad (8)$$

$\hbar$ is the reduced Planck constant. We note that $n_a = ck_a/\omega_a$ gives the index of refraction of field a. The creation and annihilation operators fulfil the usual boson commutation relations appropriate for the quantization of photon flux [52, 53],

$$[\hat{a}_a(\mathbf{k}_a^\perp, \omega_a), \hat{a}_{a'}^\dagger(\mathbf{k'}_{a'}^\perp, \omega'_{a'})] = \delta_{aa'}\delta(\mathbf{k}_a^\perp - \mathbf{k'}_{a'}^\perp)$$
$$\times \delta(\omega_a - \omega_{a'}), \quad (9)$$

where δ means the Dirac δ function and $\delta_{aa'}$ stands for the Kronecker symbol.

Substituting expressions (3) and (7) into Eq. (1) for momentum operator $\hat{G}_{int}$ we arrive at the formula

$$\hat{G}_{int}(z) = -\frac{2\hbar d_{eff}}{\sqrt{2\pi}^3 c^2} \int d\mathbf{k}_s^\perp \int d\mathbf{k}_i^\perp \int_0^\infty d\omega_s \int_0^\infty d\omega_i$$
$$\int_0^\infty d\omega_p \, \delta(\omega_p - \omega_s - \omega_i) E_p^\parallel(\omega_p) \frac{\omega_s \omega_i}{\sqrt{k_s k_i}} T_L(\mathbf{k}_s^\perp, \mathbf{k}_i^\perp)$$
$$\times \exp\left(i[k_p(\omega_s + \omega_i) - k_s(\omega_s) - k_i(\omega_i)]z\right)$$
$$\times \hat{a}_s^\dagger(\mathbf{k}_s^\perp, \omega_s, z)\hat{a}_i^\dagger(\mathbf{k}_i^\perp, \omega_i, z) + \text{H.c.}, \quad (10)$$

where d_{eff} is an effective nonlinear coefficient. Function T_L describes correlations between the signal and idler fields in the transverse wave-vector plane:

$$T_L(\mathbf{k}_s^\perp, \mathbf{k}_i^\perp) = \int d\mathbf{k}_p^\perp \delta(\mathbf{k}_p^\perp - \mathbf{k}_s^\perp - \mathbf{k}_i^\perp) E_p^\perp(\mathbf{k}_p^\perp)$$
$$\times \frac{1}{L} \int_0^L dz \exp\left(-i\left[\frac{|\mathbf{k}_p^\perp|^2}{2k_p} - \frac{|\mathbf{k}_s^\perp|^2}{2k_s} - \frac{|\mathbf{k}_i^\perp|^2}{2k_i}\right]z\right); (11)$$

$|\mathbf{k}_a^\perp|^2 = k_{a,x}^2 + k_{a,y}^2$. We note that an average value of the phase mismatch determined along the crystal of length L occurs in formula (11).

These correlations are conveniently expressed using dual ortho-normal transverse modes of the signal and idler fields. These modes are revealed by the Schmidt decomposition of the normalized function T_L^n, $T_L = t^\perp T_L^n$ and $t^{\perp 2} = \int d\mathbf{k}_s^\perp \int d\mathbf{k}_i^\perp |T_L(\mathbf{k}_s^\perp, \mathbf{k}_i^\perp)|^2$. As we are interested in the radially symmetric geometry, the use of radial variables $k_a^\perp$ and φ_a is convenient $[\mathbf{k}_a^\perp = (k_a^\perp \cos(\varphi_a), k_a^\perp \sin(\varphi_a))]$. We note that the considered radial symmetry is broken for narrow pump beams owing to the crystal anisotropy [54–56]. In the radially symmetric geometry, the normalized function T_L^n can be rewritten into the form:

$$T_L^n(\mathbf{k}_s^\perp, \mathbf{k}_i^\perp) = \frac{1}{2\pi} \sum_{m=-\infty}^\infty T_{L,m}(k_s^\perp, k_i^\perp) \exp[im(\varphi_s - \varphi_i)]. \quad (12)$$

Functions $T_{L,m}$ introduced in Eq. (12) and defined as

$$T_{L,m}(k_s^\perp, k_i^\perp) = \int_0^{2\pi} d(\varphi_s - \varphi_i) T_L^n(\mathbf{k}_s^\perp, \mathbf{k}_i^\perp)$$
$$\times \exp[-im(\varphi_s - \varphi_i)] \quad (13)$$

can be decomposed as follows:

$$\sqrt{k_{\rm s}^\perp k_{\rm i}^\perp}\, T_{L,m}(k_{\rm s}^\perp, k_{\rm i}^\perp) = \sum_{l=0}^\infty \lambda_{ml}^\perp u_{{\rm s},ml}(k_{\rm s}^\perp) u_{{\rm i},ml}(k_{\rm i}^\perp).$$
(14)

Eigenfunctions $u_{{\rm s},ml}$ and $u_{{\rm i},ml}$ form the ortho-normal dual bases and $\lambda_{ml}^\perp$ denote the corresponding eigenvalues. Substituting Eq. (14) into Eq. (12) we reveal the Schmidt decomposition of the normalized function T_L^n:

$$\sqrt{k_{\rm s}^\perp k_{\rm i}^\perp}\, T_L^n(k_{\rm s}^\perp, \varphi_{\rm s}, k_{\rm i}^\perp, \varphi_{\rm i}) = \sum_{m=-\infty}^\infty \sum_{l=0}^\infty \lambda_{ml}^\perp t_{{\rm s},ml}(k_{\rm s}^\perp, \varphi_{\rm s})$$
$$\times\, t_{{\rm i},ml}(k_{\rm i}^\perp, \varphi_{\rm i}).$$
(15)

The transverse mode functions $t_{{\rm s},ml}$ and $t_{{\rm i},ml}$ occurring in Eq. (15) take the form:

$$t_{{\rm s},ml}(k_{\rm s}^\perp, \varphi_{\rm s}) = \frac{u_{{\rm s},ml}(k_{\rm s}^\perp)\exp(im\varphi_{\rm s})}{\sqrt{2\pi}},$$
$$t_{{\rm i},ml}(k_{\rm i}^\perp, \varphi_{\rm i}) = \frac{u_{{\rm i},ml}(k_{\rm i}^\perp)\exp(-im\varphi_{\rm i})}{\sqrt{2\pi}}.$$
(16)

Introduction of field operators $\hat{a}_{a,ml}(\omega_a, z)$ related to transverse mode functions $t_{a,ml}$,

$$\hat{a}_{a,ml}(\omega_a, z) = \int_0^\infty dk_a^\perp \int_0^{2\pi} d\varphi_a\, t_{a,ml}^*(k_a^\perp, \varphi_a)$$
$$\times\, \hat{a}_a(k_a^\perp, \varphi_a, \omega_a, z), \qquad a = {\rm s, i}, \quad (17)$$

allows to rewrite the interaction momentum operator $\hat{G}_{\rm int}$ in Eq. (10) as follows:

$$\hat{G}_{\rm int}(z) = -\frac{2\hbar d_{\rm eff} t^\perp}{\sqrt{2\pi}^3 c^2} \sum_{m,l} \lambda_{ml}^\perp \int_0^\infty d\omega_{\rm s} \int_0^\infty d\omega_{\rm i}\, \frac{\omega_{\rm s}\omega_{\rm i}}{\sqrt{k_{\rm s} k_{\rm i}}}$$
$$\times\, E_{\rm p}^\parallel(\omega_{\rm s}+\omega_{\rm i}) \exp\left(i[k_{\rm p}(\omega_{\rm s}+\omega_{\rm i}) - k_{\rm s}(\omega_{\rm s}) - k_{\rm i}(\omega_{\rm i})]z\right)$$
$$\times\, \hat{a}_{{\rm s},ml}^\dagger(\omega_{\rm s}, z)\hat{a}_{{\rm i},ml}^\dagger(\omega_{\rm i}, z) + {\rm H.c.} \quad (18)$$

If the nonlinear interaction is weak, we can obtain a perturbation solution of the corresponding Schrödinger equation and express the output state $|\psi\rangle_{\rm out}$ in the form:

$$|\psi\rangle_{\rm out} = -\frac{i}{\hbar} \int_0^L dz\, \hat{G}_{\rm int}(z)|\psi\rangle_{\rm in}, \qquad (19)$$

where $|\psi\rangle_{\rm in}$ is the input signal and idler state. Substitution of Eq. (18) into Eq. (19) and consideration of the input vacuum state $|{\rm vac}\rangle$ result in the formula

$$|\psi\rangle_{\rm out} = t^\perp \sum_{m,l} \lambda_{ml}^\perp \int_0^\infty d\omega_{\rm s} \int_0^\infty d\omega_{\rm i}\, F_L(\omega_{\rm s}, \omega_{\rm i})$$
$$\times\, \hat{a}_{{\rm s},ml}^\dagger(\omega_{\rm s}, 0)\hat{a}_{{\rm i},ml}^\dagger(\omega_{\rm i}, 0)|{\rm vac}\rangle, \qquad (20)$$

where

$$F_L(\omega_{\rm s}, \omega_{\rm i}) = \frac{2id_{\rm eff}}{\sqrt{2\pi}^3 c^2} \frac{\omega_{\rm s}\omega_{\rm i}}{\sqrt{k_{\rm s}k_{\rm i}}} E_{\rm p}^\parallel(\omega_{\rm s}+\omega_{\rm i})$$
$$\times \int_0^L dz \exp\left(i[k_{\rm p}(\omega_{\rm s}+\omega_{\rm i}) - k_{\rm s}(\omega_{\rm s}) - k_{\rm i}(\omega_{\rm i})]z\right). \quad (21)$$

We note that the vacuum state $|{\rm vac}\rangle$ is omitted in the expression for the output state $|\psi\rangle_{\rm out}$ in Eq. (20).

Using eigenfunctions $f_{{\rm s},q}$ and $f_{{\rm i},q}$ and eigenvalues $\lambda_q^\parallel$ of the Schmidt decomposition of the normalized function F_L^n [$F_L = f^\parallel F_L^n$, $f^{\parallel 2} = \int d\omega_{\rm s} \int d\omega_{\rm i}|F_L(\omega_{\rm s}, \omega_{\rm i})|^2$], we can rewrite Eq. (21) as follows:

$$F_L(\omega_{\rm s}, \omega_{\rm i}) = f^\parallel \sum_{q=0}^\infty \lambda_q^\parallel f_{{\rm s},q}(\omega_{\rm s}) f_{{\rm i},q}(\omega_{\rm i}). \qquad (22)$$

New field operators $\hat{a}_{a,mlq}$ defined as

$$\hat{a}_{a,mlq} = \int_0^\infty d\omega_a\, f_{a,q}^*(\omega_a)\hat{a}_{a,ml}(\omega_a, 0), \quad a = {\rm s, i},$$
(23)

provide a simple formula for the output state $|\psi\rangle_{\rm out}$:

$$|\psi\rangle_{\rm out} = t^\perp f^\parallel \sum_{m,l,q} \lambda_{ml}^\perp \lambda_q^\parallel \hat{a}_{{\rm s},mlq}^\dagger \hat{a}_{{\rm i},mlq}^\dagger |{\rm vac}\rangle. \qquad (24)$$

According to Eq. (24) the output state $|\psi\rangle_{\rm out}$ is composed of photon pairs in independent paired modes numbered by indices (m, l, q) with probability amplitudes $t^\perp f^\parallel \lambda_{ml}^\perp \lambda_q^\parallel$.

Using the paired modes revealed both in the transverse wave-vector plane and spectrum we rewrite the 'averaged' momentum operator $\int_0^L dz \hat{G}_{\rm int}(z)/L$ from Eq. (18) into the form:

$$\hat{G}_{\rm int}^{\rm av}(z) = -\frac{i\hbar t^\perp f^\parallel}{L} \sum_{m=-\infty}^\infty \sum_{l,q=0}^\infty \lambda_{ml}^\perp \lambda_q^\parallel \hat{a}_{{\rm s},mlq}^\dagger(z)\hat{a}_{{\rm i},mlq}^\dagger(z)$$
$$+ {\rm H.c.} \qquad (25)$$

using the operators $\hat{a}_{a,mlq}$ defined in Eq. (23). The crucial advantage of the 'averaged' momentum operator $\hat{G}_{\rm int}^{\rm av}$ is that it 'diagonalizes' the nonlinear interaction leaving the separated Heisenberg equations for each pair of modes. We note that some of the paired modes are degenerate in certain symmetric configurations (e.g. collinear spectrally-degenerate emission) in the sense that both the signal and idler photons are emitted into the same spatio-spectral mode [57]. However, we do not consider explicitly such modes here. Considering an (m, l, q)-th mode, the Heisenberg equations are written as follows:

$$\frac{d\hat{a}_{{\rm s},mlq}(z)}{dz} = K_{mlq}\hat{a}_{{\rm i},mlq}^\dagger(z),$$
$$\frac{d\hat{a}_{{\rm i},mlq}(z)}{dz} = K_{mlq}\hat{a}_{{\rm s},mlq}^\dagger(z) \qquad (26)$$

using effective nonlinear coupling constants K_{mlq},

$$K_{mlq} = \frac{t^\perp f^\parallel}{L} \lambda_{ml}^\perp \lambda_q^\parallel. \qquad (27)$$

The solution of linear equations (26) for an (m, l, q)-th mode and the crystal of length L takes a simple form:

$$\hat{a}_{s,mlq}(L) = \cosh(K_{mlq}L)\hat{a}_{s,mlq}(0)$$
$$+ \sinh(K_{mlq}L)\hat{a}^\dagger_{i,mlq}(0),$$
$$\hat{a}_{i,mlq}(L) = \cosh(K_{mlq}L)\hat{a}_{i,mlq}(0)$$
$$+ \sinh(K_{mlq}L)\hat{a}^\dagger_{s,mlq}(0). \quad (28)$$

The solution for a given transverse mode (m, l) can be conveniently expressed in the matrix form:

$$\hat{\mathbf{a}}_{s,ml}(L) = \mathbf{U}_{s,ml}\hat{\mathbf{a}}_{s,ml}(0) + \mathbf{V}_{ml}\hat{\mathbf{a}}^\dagger_{i,ml}(0),$$
$$\hat{\mathbf{a}}_{i,ml}(L) = \mathbf{U}_{i,ml}\hat{\mathbf{a}}_{i,ml}(0) + \mathbf{V}^\dagger_{ml}\hat{\mathbf{a}}^\dagger_{s,ml}(0). \quad (29)$$

The matrices $\mathbf{U}_{s,ml}$, $\mathbf{U}_{i,ml}$ and $\mathbf{V}_{ml}$ introduced in Eq. (29) are written in their singular-valued decompositions as follows:

$$\mathbf{U}_{a,ml} = \mathbf{F}_{a,ml}\mathbf{\Lambda}^U_{ml}\mathbf{F}^T_{a,ml}, \quad a = s, i,$$
$$\mathbf{V}_{ml} = \mathbf{F}_{s,ml}\mathbf{\Lambda}^V_{ml}\mathbf{F}^\dagger_{i,ml}. \quad (30)$$

Columns of the matrices $\mathbf{F}_{s,ml}$ ($\mathbf{F}_{i,ml}$) in Eq. (30) are given by eigenmodes $f_{s,q}$ ($f_{i,q}$) of the Schmidt decomposition written in Eq. (22). Elements of the diagonal matrices $\mathbf{\Lambda}^U_{ml}$ and $\mathbf{\Lambda}^V_{ml}$ are derived from the solution given in Eq. (28),

$$\mathbf{\Lambda}^U_{ml,qq} = U_{mlq} = \cosh(K_{mlq}L),$$
$$\mathbf{\Lambda}^V_{ml,qq} = V_{mlq} = \sinh(K_{mlq}L). \quad (31)$$

The solution (28) allows to derive the mean values of experimental physical quantities. Spectral and temporal quantities are determined in Sec. 3 below. Spatial quantities are defined in Appendix A. Numbers of modes constituting the twin beam are described in Sec. 4.

We note that the numerical results obtained in [34] show that mild broadening of the modes determined from the perturbation solution of the Schrödinger equation occurs for strong pumping of the nonlinear process.

We also note that, in the considered radially symmetric non-collinear geometry with the pump field at normal incidence, the signal and idler fields propagate along the radial emission angles ϑ_s and ϑ_i, respectively. The central radial emission angles ϑ^0_s and ϑ^0_i corresponding to the central frequencies ω^0_s and ω^0_i are given by the conservation of energy and transverse wave vectors:

$$\omega^0_s = \omega^0_p - \omega^0_i, \quad k^0_s \sin(\vartheta^0_s) = k^0_i \sin(\vartheta^0_i), \quad (32)$$

$k^0_a = k_a(\omega^0_a)$. The central transverse wave vectors $k^{\perp 0}_a$ are then given as $k^{\perp 0}_a = k^0_a \cos(\vartheta^0_a)$, $a = s, i$. Paraxial approximation along the radial emission angle ϑ^0_a provides the following formula for wave vector $\mathbf{k}_a$ ($a = s, i$):

$$\mathbf{k}_a = \Big([k^{\perp 0}_a + \delta k_a] \cos(\varphi_a), [k^{\perp 0}_a + \delta k_a] \sin(\varphi_a),$$
$$\Big[k_a - \frac{\delta k^2_a \cos(\vartheta^0_s)^2}{2k_a}\Big] \cos(\vartheta^0_s) \Big), \quad (33)$$

where δk_a gives the declination of the transverse wave vector of field a. The derived formulas valid for the close-to-collinear geometry can be applied in general also in the non-collinear case provided that the following formal substitution is used:

$$k_a \longleftarrow k_a \cos(\vartheta^0_s), \delta k_a \longleftarrow \delta k_a \cos(\vartheta^0_s)^2. \quad (34)$$

III. SPECTRAL AND TEMPORAL PROPERTIES OF TWIN BEAMS

We assume that the transverse profiles of twin beams are not experimentally resolved and so the experimental mean values are obtained by averaging over the transverse modes. Then the signal-field intensity spectrum $n_{s,\omega}$ is expressed as follows:

$$n_{s,\omega}(\omega_s) = \langle \hat{a}^\dagger_s(\omega_s, L)\hat{a}_s(\omega_s, L)\rangle_\perp$$
$$= \sum_{ml}\sum_q |f_{s,q}(\omega_s)|^2 V^2_{mlq}. \quad (35)$$

Symbol $\langle\rangle_\perp$ denotes quantum mechanical averaging combined with averaging in the transverse plane. The number N_s of generated signal photons is determined along the formula

$$N_s = \int_0^\infty d\omega_s\, n_{s,\omega}(\omega_s) = \sum_{ml}\sum_q V^2_{mlq}. \quad (36)$$

Averaged signal-field intensity spectral correlations are characterized by the fourth-order correlation function $A_{s,\omega}$ given as:

$$A_{s,\omega}(\omega_s, \omega'_s) = \langle \mathcal{N} : \Delta[\hat{a}^\dagger_s(\omega_s, L)\hat{a}_s(\omega_s, L)]$$
$$\times \Delta[\hat{a}^\dagger_s(\omega'_s, L)\hat{a}_s(\omega'_s, L)] :\rangle_\perp$$
$$= \sum_{ml} |A^a_{s,ml,\omega}(\omega_s, \omega'_s)|^2. \quad (37)$$

The signal-field amplitude correlation function $A^a_{s,ml,\omega}$ belonging to mode (m, l) is written in the form:

$$A^a_{s,ml,\omega}(\omega_s, \omega'_s) = \langle \hat{a}^\dagger_s(\omega_s, L)\hat{a}_s(\omega'_s, L)\rangle_{\perp,ml}$$
$$= \sum_q f^*_{s,q}(\omega_s)f_{s,q}(\omega'_s)V^2_{mlq}. \quad (38)$$

Intensity spectral cross-correlations between the signal and idler fields are quantified by the following fourth-order correlation function:

$$C_\omega(\omega_s, \omega_i) = \langle \mathcal{N} : \Delta[\hat{a}^\dagger_s(\omega_s, L)\hat{a}_s(\omega_s, L)]$$
$$\times \Delta[\hat{a}^\dagger_i(\omega_i, L)\hat{a}_i(\omega_i, L)] :\rangle_\perp$$
$$= \sum_{ml} \left| \sum_q f_{s,q}(\omega_s)f_{i,q}(\omega_i)U_{mlq}V_{mlq} \right|^2. \quad (39)$$

Temporal electric-field amplitude and intensity correlations in the twin beams outside the nonlinear crystal

can be expressed, similarly as their spectral correlations, in terms of temporal eigenfunctions $\tilde{f}_{a,q}(t_a)$ determined by the Fourier transform:

$$\tilde{f}_{a,q}(t_a) = \sqrt{\frac{\hbar}{2\pi}} \int d\omega_a \sqrt{\omega_a} f_{a,q}(\omega_a) \exp(-i\omega_a t_a). \quad (40)$$

The averaged signal-field photon flux $I_{s,t}$ is then derived in terms of functions $\tilde{f}_{s,q}$,

$$I_{s,t}(t_s) = 2\epsilon_0 c \langle \hat{E}_s^{(-)}(\mathbf{r}_s^\perp, L, t_s) \hat{E}_s^{(+)}(\mathbf{r}_s^\perp, L, t_s) \rangle_\perp$$
$$= \sum_{ml} \sum_q |\tilde{f}_{s,q}(t_s)|^2 V_{mlq}^2. \quad (41)$$

The averaged signal-field intensity temporal correlation function $A_{s,t}$ is expressed similarly as the spectral correlation function $A_{s,\omega}$ given in Eq. (37),

$$A_{s,t}(t_s, t_s') = (2\epsilon_0 c)^2 \langle \mathcal{N} : \Delta[\hat{E}_s^{(-)}(\mathbf{r}_s^\perp, L, t_s)$$
$$\times \hat{E}_s^{(+)}(\mathbf{r}_s^\perp, L, t_s)]\Delta[\hat{E}_s^{(-)}(\mathbf{r}_s^\perp, L, t_s')\hat{E}_s^{(+)}(\mathbf{r}_s^\perp, L, t_s')] :\rangle_\perp$$
$$= \sum_{ml} \left| A_{s,ml,t}^{a}(t_s, t_s') \right|^2. \quad (42)$$

The signal-field amplitude temporal correlation function $A_{s,ml,t}^{a}$ of mode (m,l) is determined along the formula

$$A_{s,ml,t}^{a}(t_s, t_s') = 2\epsilon_0 c \langle \hat{E}_s^{(-)}(\mathbf{r}_s^\perp, L, t_s) \hat{E}_s^{(+)}(\mathbf{r}_s^\perp, L, t_s') \rangle_{\perp,ml}$$
$$= \sum_q \tilde{f}_{s,q}^*(t_s) \tilde{f}_{s,q}(t_s') V_{mlq}^2. \quad (43)$$

Also the averaged intensity temporal cross-correlations between the signal and idler fields can be quantified in the same vein as in Eq. (39):

$$C_t(t_s, t_i) = (2\epsilon_0 c)^2 \langle \mathcal{N} : \Delta[\hat{E}_s^{(-)}(\mathbf{r}_s^\perp, L, t_s)$$
$$\times \hat{E}_s^{(+)}(\mathbf{r}_s^\perp, L, t_s)]\Delta[\hat{E}_i^{(-)}(\mathbf{r}_i^\perp, L, t_i)\hat{E}_i^{(+)}(\mathbf{r}_i^\perp, L, t_i)] :\rangle_\perp$$
$$= \sum_{ml} \left| \sum_q \tilde{f}_{s,q}(t_s) \tilde{f}_{i,q}(t_i) U_{mlq} V_{mlq} \right|^2. \quad (44)$$

As the number of transverse modes is usually large, their eigenvalues $\lambda_{ml}^\perp$ form quasi-continuum. In this case, we may introduce a suitable probability function ϱ_λ and make the following replacement in the above formulas:

$$\sum_{ml} \longrightarrow \int_0^1 d\lambda^\perp \varrho_\lambda(\lambda^\perp). \quad (45)$$

This makes the numerical computations considerably faster.

The mode $(m,l,q) = (0,0,0)$ having the largest value of the product $\lambda^\perp \lambda^\parallel$ of the Schmidt eigenvalues becomes dominant in the limit of large pump power $(P_p \to \infty)$ in the used un-depleted pump approximation. The spectral characteristics $n_{s,\omega}$, $A_{s,\omega}$ and $C_{s,\omega}$ then attain the simple form:

$$n_{s,\omega}(\omega_s) = N_s |f_{s,0}(\omega_s)|^2,$$
$$A_{s,\omega}(\omega_s, \omega_s') = N_s^2 |f_{s,0}(\omega_s)|^2 |f_{s,0}(\omega_s')|^2,$$
$$C_\omega(\omega_s, \omega_i) = \lambda_{00}^{\perp 2} U_{00,0}^2 V_{00,0}^2 |f_{s,0}(\omega_s)|^2 |f_{i,0}(\omega_i)|^2, \quad (46)$$

where $N_s = V_{00,0}^2$ gives the number of emitted signal photons. According to Eqs. (46), the twin beam is spectrally composed of independent single-mode signal and idler fields in this high-intensity (classical) limit. We note that one dominant paired mode constitutes the twin beam also in the transverse wave-vector plane and the crystal output plane. So the signal and idler fields are spatially and spectrally independent but internally fully spatially and spectrally coherent.

Similar quantities as defined above in the spectral and temporal domains are used for describing the twin beams in their transverse wave-vector plane and crystal output plane. Modes in the crystal output plane are determined from those of the transverse wave-vector plane using the Fourier transform, similarly as the temporal modes have been derived from the spectral modes. The radial symmetry of twin beams results in harmonic azimuthal modes in the crystal output plane. It also provides the radial modes in the crystal output plane determined from those of the transverse wave-vector plane using the transformation based on the Bessel functions (for details, see Appendix A).

IV. DIMENSIONALITY OF THE TWIN BEAM

Dimensionality of a twin beam can be determined either using its paired properties or properties of the individual signal and idler fields. In the first case, dimensionality of entanglement is obtained. In the second case, the numbers of independent modes constituting the signal (or idler) field and defined in statistical optics are reached. Entanglement dimensionality for a general noisy twin beam is quantified via negativity [58]. Considering pure states of the noiseless twin beams, the Schmidt number can be applied for quantifying entanglement dimensionality as well [23, 24]. This number can even be reached without making the Schmidt decomposition [59, 60]. The general formulas can be recast into a simple form for quasi-monochromatic or quasi-homogeneous fields [61].

Compared to weak fields, the analysis of intense twin beams is more difficult, as the decompositions not only in the spatial and spectral domains but also in the Hilbert spaces of individual paired spatio-spectral modes spanned by the Fock-number states would be needed. That is why, we apply here a simpler approach for determining entanglement dimensionality based upon defining creation operators for photon pairs (for details, see [36]). Entanglement dimensionality K of the twin beam is obtained in this approach as follows:

$$K = \frac{\left(\sum_{mlq} U_{mlq}^2 V_{mlq}^2 \right)^2}{\sum_{mlq} U_{mlq}^4 V_{mlq}^4}. \quad (47)$$

We note that formula (47) reduces to the usually used Schmidt number of spatio-spectral modes for weak twin beams.

Formula (47) can also be applied to provide average number K_ω of effectively populated paired spectral modes:

$$K_\omega = \sum_{ml} p_{ml}^\perp \frac{\left(\sum_q U_{mlq}^2 V_{mlq}^2\right)^2}{\sum_q U_{mlq}^4 V_{mlq}^4}. \qquad (48)$$

In Eq. (47), $p_{ml}^\perp$ gives the probability of having a photon pair in mode (m, l):

$$p_{ml}^\perp = \frac{\sum_q V_{mlq}^2}{\sum_{mlq} V_{mlq}^2}. \qquad (49)$$

Similarly as in the spectrum, average number $K_{k\varphi}$ of effectively populated modes in the transverse wave-vector plane is obtained along the formula:

$$K_{k\varphi} = \sum_q p_q^\parallel \frac{\left(\sum_{ml} U_{mlq}^2 V_{mlq}^2\right)^2}{\sum_q U_{mlq}^4 V_{mlq}^4} \qquad (50)$$

using probability $p_{ml}^\parallel$ of having a photon pair in mode q;

$$p_q^\parallel = \frac{\sum_{ml} V_{mlq}^2}{\sum_{mlq} V_{mlq}^2}. \qquad (51)$$

The numbers K_ω and $K_{k\varphi}$ of paired modes in the spectrum and transverse wave-vector plane, respectively, can alternatively be determined as the ratio of the width Δn_s of, say, the signal-field intensity profile and the width of intensity cross-correlation function ΔC in the appropriate variable. This ratio known as the Fedorov ratio [62] coincides with the number K_ω of paired modes given in Eq. (48) for weak twin beams with a Gaussian two-photon amplitude [63]. It has been shown in [64] that both numbers are close to each other for general weak twin beams.

Modes in the signal and idler fields are ideally paired as well as the signal and idler photons in individual spatio-spectral modes for the considered noiseless twin beams. That is why, dimensionality of the twin beam can also be determined from the number of modes and their populations counted either in the signal or idler field. Applying the coherence theory [65], an effective number of independent modes (degrees of freedom) in the signal (or idler) field can be obtained from its photon-number statistics. The resulting number K^n of modes constituting, e.g., the signal field is given by the formula valid for a multimode thermal field [66]:

$$K^n = \frac{\left(\sum_{mlq} \langle \hat{n}_{s,mlq} \rangle\right)^2}{\sum_{mlq} \left(\langle \mathcal{N} : \hat{n}_{s,mlq}^2 : \rangle - \langle \hat{n}_{s,mlq} \rangle^2\right)}$$
$$= \frac{\left(\sum_{mlq} V_{mlq}^2\right)^2}{\sum_{mlq} V_{mlq}^4}; \qquad (52)$$

$\hat{n}_{s,mlq} \equiv \hat{a}_{s,mlq}^\dagger(L) \hat{a}_{s,mlq}(L)$.

Also, the formula for averaged number K_ω^n of spectral modes can be written, in analogy with the derivation of Eq. (48) from Eq. (47):

$$K_\omega^n = \sum_{ml} p_{ml}^\perp K_{\omega,ml}^n, \qquad (53)$$

$$K_{\omega,ml}^n = \frac{\left(\sum_q \langle \hat{n}_{s,mlq} \rangle\right)^2}{\sum_q \left(\langle \mathcal{N} : \hat{n}_{s,mlq}^2 : \rangle - \langle \hat{n}_{s,mlq} \rangle^2\right)}$$
$$= \frac{\left(\sum_q V_{mlq}^2\right)^2}{\sum_q V_{mlq}^4}.$$

The averaged number $K_{k\varphi}^n$ of modes in the transverse wave-vector plane can be determined by a formula analogous to that written in Eq. (53) [compare Eqs. (48) and (50).

The ratio K_s^Δ of the width Δn_s of a signal-field intensity profile and the width ΔA_s^a of the appropriate signal-field amplitude auto-correlation function,

$$K_s^\Delta = \frac{\Delta n_s}{\Delta A_s^a}, \qquad (54)$$

defined in any variable represents also a good quantifier of the number of independent modes of a twin beam in this variable. We compare different quantifiers of dimensionality of the twin beam under real experimental conditions below.

V. SPECTRAL AND TEMPORAL PROPERTIES OF INTENSE TWIN BEAMS

In the numerical analysis, we consider a BBO crystal 8-mm long cut for non-collinear type I process (eoo) for the spectrally-degenerate interaction pumped by the pulse at wavelength $\lambda_p = 349$ nm with spectral width $\Delta\lambda_p = 0.1$ nm, transverse profile with radius $w_p = 1$ mm and repetition rate $f = 400$ s^{-1}. This pulse is provided by the third harmonics of the Nd:YLF laser at wavelength 1.047 μm. Assuming the pump field at normal incidence, the signal and idler fields at the central wavelengths $\lambda_s^0 = \lambda_i^0 = 698$ nm ($\vartheta_{BBO} = 36.3$ deg) propagate outside the crystal under the radial emission angles $\vartheta_s^0 = \vartheta_i^0 = 8.45$ deg. As this configuration is symmetric for the signal and idler fields, we further discuss only the properties of signal field. We assume that the conditions are such that the spectral and spatial properties of the twin beam factorize.

The generated twin beam is composed of roughly 80 thousand transverse modes at low intensity. It contains 34 modes in radial direction and 2350 modes in azimuthal direction (for more details, see [56]). As the number of transverse modes is large, we can introduce quasi-continuum of the Schmidt eigenvalues with its probability function ϱ_λ defined in Eq. (45). The probability
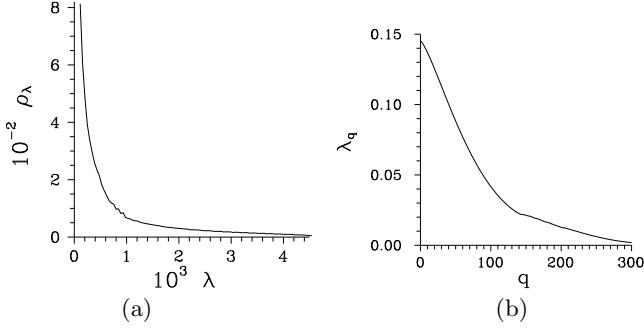
8

FIG. 1. (a) Probability function ϱ_λ of eigenvalues $\lambda_{ml}^\perp$ in the transverse wave-vector plane and (b) spectral eigenvalues λ_q; $w_p = 1 \times 10^{-3}$ m, $\Delta\lambda_p = 1 \times 10^{-10}$ m.
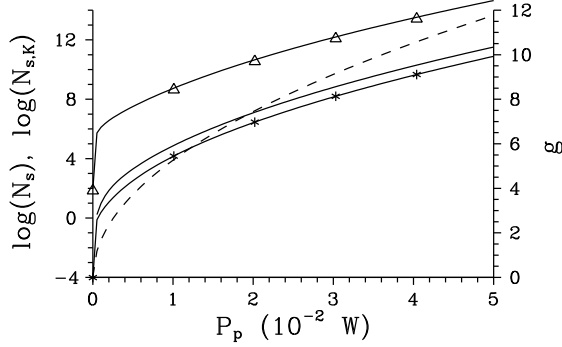

FIG. 2. Number N_s of emitted signal photons (solid curve with $\triangle$), number N_{s,K^n} of emitted signal photons per mode defined by photon-number statistics (solid curve with $*$), number $N_{s,K}$ of emitted signal photons per mode given by Eq. (54) (plain curve), and gain g (dashed curve) as functions of pump power P_p; log denotes the decimal logarithm; $w_p = 1 \times 10^{-3}$ m, $\Delta\lambda_p = 1 \times 10^{-10}$ m.

function ϱ_λ is plotted in Fig. 1(a). It reflects the fact that the smaller the eigenvalue the larger the number of such eigenvalues. There occur around 80 independent spectral modes in the low-intensity regime, as shown in Fig. 1(b).

The number N_s of emitted signal photons increases roughly exponentially with the increasing pump power P_p for more intense fields [44], as shown in Fig. 2. The curves in Fig. 2 giving the number of emitted signal photons per one mode show that the probabilities of spontaneous and stimulated emissions of a signal photon (together with its idler twin) become comparable for pump powers P_p around 0.5 mW. Exponential increase of the number N_s of emitted signal photons occurs already for pump powers P_p one order of magnitude lower. It is useful to define gain g of the nonlinear interaction and to use it instead of the pump power P_p when comparing the theoretical quantities with their experimental counterparts. The gain g arises from a simplified model of the nonlinear interaction that assumes only one effective mode and the initial vacuum state of the signal and idler fields. Formulas (27), (28) and (35) of Sec. II provide in
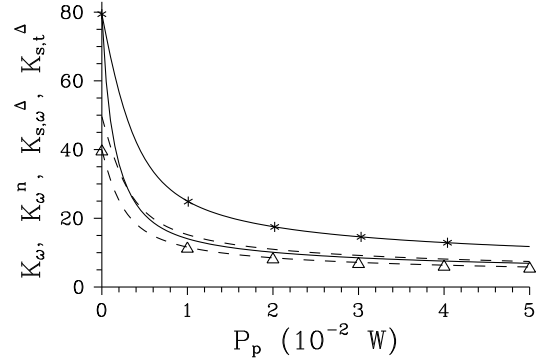

FIG. 3. Spectral entanglement dimensionality K_ω (plain solid curve), number K_ω^n of modes determined from photon-number statistics (solid curve with $*$) and number $K_{s,\omega}^\Delta$ [$K_{s,t}^\Delta$] of spectral [temporal] modes given by Eq. (54) (dashed curve [dashed curve with $\triangle$]) as functions of pump power P_p; $w_p = 1 \times 10^{-3}$ m, $\Delta\lambda_p = 1 \times 10^{-10}$ m.

this case the expression $(\lambda_{00}^\perp = \lambda_0^\parallel = 1)$

$$N_s = \sinh(t^\perp f^\parallel \sqrt{P_p})^2. \tag{55}$$

It suggests the following approximative formula for fitting the experimental dependence of the number N_s of signal photons:

$$N_s = N_{s,0} \sinh(g)^2, \tag{56}$$

where $g = g_0 \sqrt{P_p}$ and $N_{s,0}$ and g_0 are suitable constants. The values of gain g assigned to pump powers P_p are plotted in Fig. 2. They show the advantage of this parametrization: Stimulated emission of photon pairs begins to dominate over spontaneous emission for the values of gain g around one and the transition from quantum to classical regimes (mesoscopic regime) occurs for the values of gain g around 10.

Spectral entanglement dimensionality K_ω determined by formula (48) decreases with the increasing values of pump power P_p [45] (see Fig. 3). The number $K_{s,\omega}^\Delta$ of spectral signal-field modes as well as the number $K_{s,t}^\Delta$ of temporal signal-field modes given in Eq. (54) by the ratios of appropriate widths and plotted in Fig. 3 are lower than the spectral entanglement dimensionality K_ω. The comparison of curves in Fig. 3 shows that the experimentally available values of $K_{s,\omega}^\Delta$ and $K_{s,t}^\Delta$ can successfully be used for quantifying dimensionality of the twin beam, together with the theoretical entanglement dimensionality K_ω. The number of modes constituting the twin beam can also be derived from the photon-number statistics in the signal (or idler) field [50, 67, 68]. In this case, the number K_ω^n of modes is given by formula (53). It provides systematically greater numbers of modes, as the curves in Fig. 3 show. The values of entanglement dimensionality K_ω and number K_ω^n of modes nearly coincide in the low-intensity regime. This immediately follows from the comparison of Eqs. (48) and (53) in the limit $U_{mlq} \approx 1$. Also, the numbers $K_{s,\omega}^\Delta$, $K_{s,t}^\Delta$ and K_ω^n of modes equal to
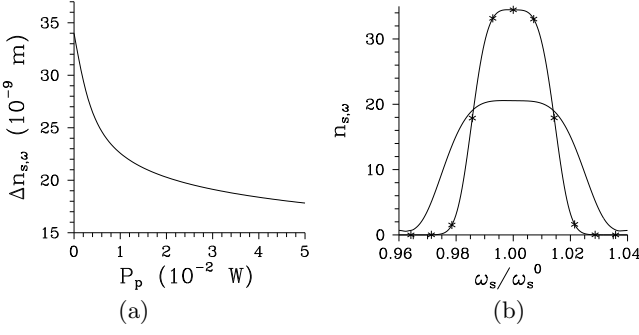
FIG. 4. (a) Width $\Delta n_{s,\omega}$ of signal-field intensity spectrum as a function of pump power P_p and (b) spectrum $n_{s,\omega}$ for $P_p = 1 \times 10^{-7}$ W (plain curve) and $P_p = 2 \times 10^{-2}$ W (solid curve with $*$); $w_p = 1 \times 10^{-3}$ m, $\Delta\lambda_p = 1 \times 10^{-10}$ m. Spectrum $n_{s,\omega}$ is normalized according to $\int d\omega_s n_{s,\omega}(\omega_s)/\omega_s^0 = 1$.
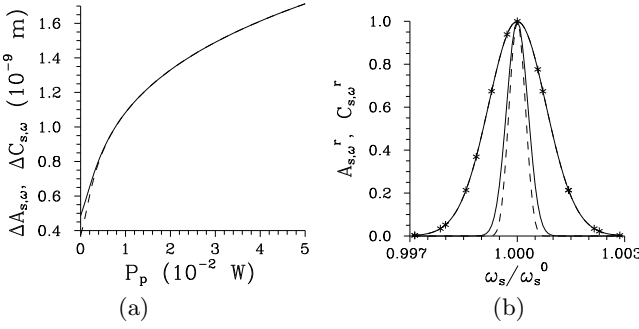

FIG. 5. (a) Widths $\Delta A_{s,\omega}$ of signal-field intensity auto-correlation function (solid curve) and $\Delta C_{s,\omega}$ of intensity cross-correlation function (dashed curve) as functions of pump power P_p. In (b), intensity auto-correlation function $A_{s,\omega}^r(\omega_s) \equiv A_{s,\omega}(\omega_s,\omega_s^0)/A_{s,\omega}(\omega_s^0,\omega_s^0)$ and cross-correlation function $C_{s,\omega}^r(\omega_s) \equiv C_{s,\omega}(\omega_s,\omega_i^0)/C_{s,\omega}(\omega_s^0,\omega_i^0)$ are plotted for $P_p = 1 \times 10^{-7}$ W (plain curves) and $P_p = 2 \times 10^{-2}$ W (nearly coinciding curves with $*$); $w_p = 1 \times 10^{-3}$ m, $\Delta\lambda_p = 1 \times 10^{-10}$ m.

the entanglement dimensionality K_ω in the high-intensity limit ($P_p \to \infty$). This occurs because the strongest mode completely dominates over the other modes in this limit.

Decrease of the number $K_{s,\omega}^\Delta$ of signal-field modes with the increasing pump power P_p originates in the behavior of spectral widths $\Delta n_{s,\omega}$ and $\Delta A_{s,\omega}^a$. Whereas the spectral width $\Delta n_{s,\omega}$ of the signal-field intensity profile decreases with the increasing pump power P_p [see Fig. 4(a)], the width $\Delta A_{s,\omega}^a$ of signal-field amplitude auto-correlation function increases [for the width $\Delta A_{s,\omega}$ of intensity auto-correlation function, see Fig. 5(a)]. This occurs because the spectral modes with greater eigenvalues λ_q become more and more important with the increasing pump power P_p. Hand in hand, the role of modes with small eigenvalues λ_q is suppressed. As the modes with large eigenvalues λ_q are localized more in the middle of the spectrum (for more details, see, e.g., [25]), narrowing of the signal-field intensity spectrum is naturally observed. This is accompanied by reshaping of the spectrum $n_{s,\omega}$ that looses small oscillating tails present
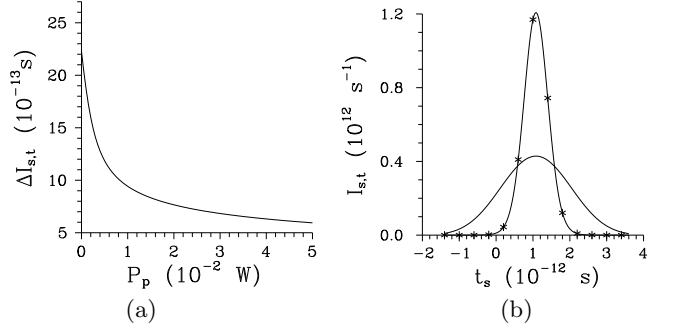

FIG. 6. (a) Width $\Delta I_{s,t}$ (FWHM) of signal-field photon flux as a function of pump power P_p and (b) photon flux $I_{s,t}$ for $P_p = 1 \times 10^{-7}$ W (plain curve) and $P_p = 2 \times 10^{-2}$ W (solid curve with $*$); $w_p = 1 \times 10^{-3}$ m, $\Delta\lambda_p = 1 \times 10^{-10}$ m. The curves in (b) are normalized such that $\int dt_s I_{s,t}(t_s) = 1$.

in the low-intensity regime [see Fig. 4(b)]. As the generation of photons by stimulated emission increases with the increasing pump power P_p, coherence in the twin beam increases. This leads to broadening of the widths $\Delta A_{s,\omega}$ and $\Delta C_{s,\omega}$ of intensity auto- and cross-correlation functions [45]. As the curves in Fig. 5(b) drawn for two different pump powers P_p show, the intensity auto-correlation function $A_{s,\omega}$ is wider than its cross-correlation counterpart $C_{s,\omega}$ in the low-intensity regime (for the explanation, see [56]). When stimulated emission begins to dominate over spontaneous emission [see Fig. 5(a)], the auto-correlation and cross-correlation functions approach each other. In the high-intensity limit $P_p \to \infty$, the signal and idler fields are single-mode and so they are spectrally coherent.

The signal field is emitted in the form of a short pulse. It is composed of the temporal modes $\tilde{f}_{s,q}$ given in Eq. (40). These modes behave similarly as their spectral counterparts [30]. Thus, a q-th mode has q maxima and $q-1$ zeroes in its intensity temporal profile. Also, the greater the number q, the wider the mode. The field transition to the high-intensity regime looks as follows. The signal pulse is in general longer than the pump pulse in the low-intensity regime [14]. However, as shown in Fig. 6(a) the signal pulse shortens with the increasing pump power P_p due to the nonlinear interaction described in momentum operator $\hat{G}_{int}$ written in Eq. (1). The signal pulse is also delayed with respect to the pump pulse [see Fig. 6(b)] as a consequence of different group velocities of two pulses inside the crystal [19]. Coherence in the signal field as well as coherence between the signal and idler fields increase with the increasing pump power P_p due to stimulated emission, as documented in Fig. 7(a). The intensity auto-correlation function $A_{s,t}$ is narrower than the intensity cross-correlation function $C_{s,t}$ in the time domain and low-intensity regime [see Fig. 7(b)]. This is opposed to the behavior of spectral correlation functions. It originates in properties of the Fourier transform. The cross-correlation and auto-correlation functions are close to each other for greater
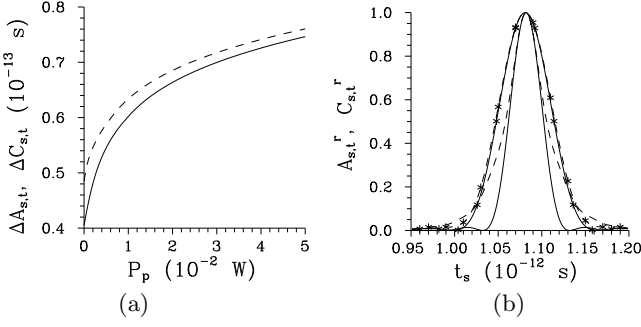
FIG. 7. (a) Widths $\Delta A_{s,t}$ (FWHM) of signal-field intensity auto-correlation function (solid curve) and $\Delta C_{s,t}$ of intensity cross-correlation function (dashed curve) depending on pump power P_p. In (b), intensity auto-correlation function $A^r_{s,t}(t_s) \equiv A_{s,t}(t_s, t^{max}_s)/A_{s,t}(t^{max}_s, t^{max}_s)$ and cross-correlation function $C^r_{s,t}(t_s) \equiv C_{s,t}(t_s, t^{max}_i)/C_{s,t}(t^{max}_s, t^{max}_i)$ are plotted for $P_p = 1 \times 10^{-7}$ W (plain curves) and $P_p = 2 \times 10^{-2}$ W (nearly coinciding curves with $*$); t^{max}_s and t^{max}_i give the times with maximal photon fluxes in the signal and idler fields, respectively; $w_p = 1 \times 10^{-3}$ m, $\Delta\lambda_p = 1 \times 10^{-10}$ m.

FIG. 8. Entanglement dimensionality $K_{k\varphi}$ (plain solid curve), number $K^n_{k\varphi}$ of signal-field modes determined from photon-number statistics (solid curve with $*$) and number $K^\Delta_{s,k\varphi}$ [$\tilde{K}^\Delta_{s,r\psi}$] of signal-field modes in the transverse wave-vector [crystal output] plane given by Eq. (54) (plain dashed curve [dashed curve with $\triangle$]) as they depend on pump power P_p. Number $\tilde{K}^\Delta_{s,r\psi}$ equals $\tilde{K}^{\Delta 2}_{s,r}$ given in Eq. (54) in which the width $\Delta\tilde{A}^a_{s,r} = 2\int^\infty_{r'_s} dr_s (r_s - r'_s) A^a_{s,r}(r_s, r'_s)/\int^\infty_{r'_s} dr_s A^a_{s,r}(r_s, r'_s)$; $w_p = 1 \times 10^{-3}$ m, $\Delta\lambda_p = 1 \times 10^{-10}$ m.

values of pump power P_p, as shown in Fig. 7(b). In the high-intensity limit $P_p \to \infty$, the twin beam is found in a separable temporally coherent state composed of the signal- and idler-field temporal modes $\tilde{f}_{s,0}$ and $\tilde{f}_{i,0}$ written in Eq. (40).

VI. PROPERTIES OF INTENSE TWIN BEAMS IN THE TRANSVERSE WAVE-VECTOR AND CRYSTAL OUTPUT PLANES

We analyze properties of the twin beam in the wave-vector transverse plane (far field) and the crystal output plane (near field) assuming spectral (or temporal) averaging.

Entanglement dimensionality $K_{k\varphi}$ in the transverse plane gives around 80 thousand modes in the low-intensity regime. It decreases with the increasing pump power P_p (see Fig. 8) [44, 45]. This behavior is similar to that found in the spectral and temporal domains. It can be explained in the same way. Entanglement dimensionality $K_{k\varphi}$ in the transverse plane and number $K^n_{k\varphi}$ of signal-field transverse modes provided by the photon-number statistics are close to each other, as shown in Fig. 8. These numbers can alternatively be experimentally estimated using the product $K^\Delta_k K^\Delta_\varphi$ of ratios of intensity widths and widths of amplitude auto-correlation functions both in radial and azimuthal transverse wave-vector directions applying formula (54). Factorization of the number of modes into its radial and azimuthal contributions is valid in our geometry in which the photons are emitted into a narrow ring in the wave-vector transverse plane. In the low-intensity limit, there is around 34 [2350] modes in radial [azimuthal] wave-vector direction. Around 10 [1000] modes are found in radial [azimuthal] wave-vector direction for the pump power $P_p = 50$ mW.
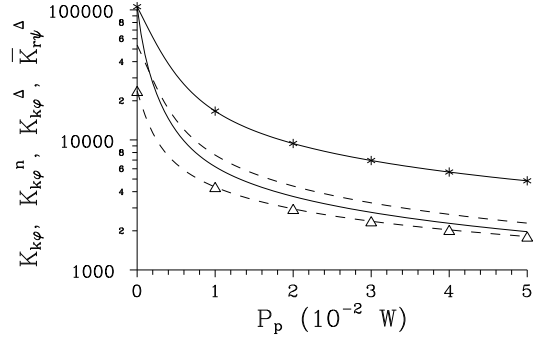
On the other hand, the signal and idler photons form a disc centered around $x = y = 0$ m in the crystal output plane. As the correlated areas in the crystal output plane are radially symmetric and practically do not change with intensity (see below), we can estimate the number of transverse modes also by the squared ratio $K^{\Delta 2}_r$ determined from the appropriate widths in radial direction. As the curves in Fig. 8 confirm, all these quantities give reasonable numbers of modes of the analyzed twin beam close to the entanglement dimensionality $K_{k\varphi}$.

In the wave-vector transverse plane, decrease of entanglement dimensionality $K_{k\varphi}$ with the increasing pump power P_p is explained by decrease of the width $\Delta n_{s,k}$ of intensity profile in radial wave-vector direction (see Fig. 9) accompanied by increase of widths $\Delta A^a_{s,k}$ and $\Delta A^a_{s,\varphi}$ of amplitude auto-correlation functions in radial and azimuthal wave-vector directions, respectively [44, 45, 69]. The ring in the transverse wave-vector plane formed by the signal photons [22] thus becomes narrower with the increasing pump power P_p, as confirmed by the radial signal-field intensity profiles $n_{s,k}$ plotted in Fig. 9(b). The behavior of intensity profile $n_{s,k}$ and intensity auto- ($A_{s,k}$) and cross-correlation ($C_{s,k}$) functions in radial wave-vector direction (see Fig. 10) resembles that found in the frequency domain. Also here the auto-correlation functions $A_{s,k}$ are broader than their cross-correlation counterparts $C_{s,k}$ for low intensities, but they approach each other for more intense twin beams (see Fig. 10). This behavior follows from qualitative similarity of mode profiles in both variables. We remind that an l-th mode in radial wave-vector direction has l maxima and $l-1$ zeroes in its intensity profile. The behavior of auto- ($A_{s,\varphi}$) and cross-correlation ($C_{s,\varphi}$) functions in the
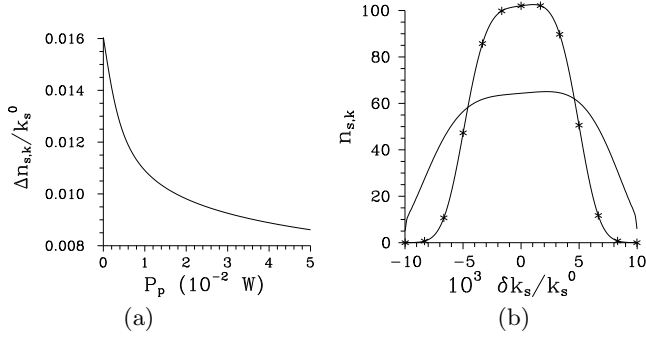
FIG. 9. (a) Width $\Delta n_{\mathrm{s},k}$ of radial signal-field intensity profile as a function of pump power P_{p} and (b) radial intensity profile $n_{\mathrm{s},k}$ for $P_{\mathrm{p}} = 1 \times 10^{-7}$ W (plain curve) and $P_{\mathrm{p}} = 2 \times 10^{-2}$ W (solid curve with $*$); $w_{\mathrm{p}} = 1 \times 10^{-3}$ m, $\Delta\lambda_{\mathrm{p}} = 1 \times 10^{-10}$ m. Intensity profile $n_{\mathrm{s},k}$ is normalized such that $\int dk_{\mathrm{s}} n_{\mathrm{s},k}(k_{\mathrm{s}})/k_{\mathrm{s}}^0 = 1$.
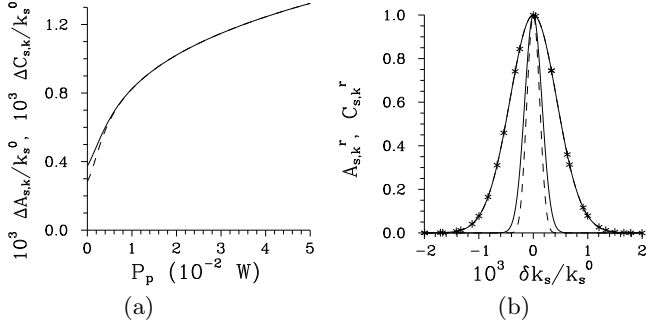

FIG. 10. (a) Widths $\Delta A_{\mathrm{s},k}$ of signal-field intensity auto-correlation function (solid curve) and $\Delta C_{\mathrm{s},k}$ of intensity cross-correlation function (dashed curve) in radial wave-vector direction as they depend on pump power P_{p}. In (b), signal-field intensity auto-correlation function $A_{\mathrm{s},k}^{\mathrm{r}}(\delta k_{\mathrm{s}}) \equiv A_{\mathrm{s},k}(k_{\mathrm{s}}^0 + \delta k_{\mathrm{s}}, k_{\mathrm{s}}^0)/A_{\mathrm{s},k}(k_{\mathrm{s}}^0, k_{\mathrm{s}}^0)$ and cross-correlation function $C_{\mathrm{s},k}^{\mathrm{r}}(\delta k_{\mathrm{s}}) \equiv C_{\mathrm{s},k}(k_{\mathrm{s}}^0 + \delta k_{\mathrm{s}}, k_{\mathrm{i}}^0)/C_{\mathrm{s},k}(k_{\mathrm{s}}^0, k_{\mathrm{i}}^0)$ are plotted for $P_{\mathrm{p}} = 1 \times 10^{-7}$ W (plain curves) and $P_{\mathrm{p}} = 2 \times 10^{-2}$ W (nearly coinciding curves with $*$); $w_{\mathrm{p}} = 1 \times 10^{-3}$ m, $\Delta\lambda_{\mathrm{p}} = 1 \times 10^{-10}$ m.

FIG. 11. (a) Widths $\Delta A_{\mathrm{s},\varphi}$ of signal-field intensity auto-correlation function (solid curve) and $\Delta C_{\mathrm{s},\varphi}$ of intensity cross-correlation function (dashed curve) in azimuthal wave-vector direction in dependence on pump power P_{p}. In (b), signal-field intensity auto-correlation function $A_{\mathrm{s},\varphi}^{\mathrm{r}}(\delta\varphi_{\mathrm{s}}) \equiv A_{\mathrm{s},\varphi}(\varphi_{\mathrm{s}}^0 + \delta\varphi_{\mathrm{s}}, \varphi_{\mathrm{s}}^0)/A_{\mathrm{s},\varphi}(\varphi_{\mathrm{s}}^0, \varphi_{\mathrm{s}}^0)$ valid for an arbitrary φ_{s}^0 and cross-correlation function $C_{\mathrm{s},\varphi}^{\mathrm{r}}(\delta\varphi) \equiv C_{\mathrm{s},\varphi}(\varphi_{\mathrm{s}}^0 + \delta\varphi, \varphi_{\mathrm{i}}^0)/C_{\mathrm{s},\varphi}(\varphi_{\mathrm{s}}^0, \varphi_{\mathrm{i}}^0)$ given for an arbitrary $\varphi_{\mathrm{i}}^0 = \varphi_{\mathrm{s}}^0 + \pi$ are shown for $P_{\mathrm{p}} = 1 \times 10^{-7}$ W (plain curves) and $P_{\mathrm{p}} = 2\times 10^{-2}$ W (nearly coinciding curves with $*$); $w_{\mathrm{p}} = 1\times 10^{-3}$ m, $\Delta\lambda_{\mathrm{p}} = 1 \times 10^{-10}$ m.

FIG. 12. (a) Width $\Delta n_{\mathrm{s},r}$ of radial signal-field intensity profile in the crystal output plane of as a function of pump power P_{p} and (b) radial intensity profile $n_{\mathrm{s},r}$ for $P_{\mathrm{p}} = 1 \times 10^{-7}$ W (plain curve) and $P_{\mathrm{p}} = 2 \times 10^{-2}$ W (solid curve with $*$); $w_{\mathrm{p}} = 1 \times 10^{-3}$ m, $\Delta\lambda_{\mathrm{p}} = 1 \times 10^{-10}$ m. Intensity profile $n_{s,r}$ is normalized such that $\int_0^\infty dr_{\mathrm{s}} r_{\mathrm{s}} n_{\mathrm{s},r}(r_{\mathrm{s}}) = 1/2$.

azimuthal wave-vector direction is similar to that found in the radial wave-vector direction (see Fig. 11).

Contrary to the transverse wave-vector plane, decrease of entanglement dimensionality $K_{r\psi}$ with the increasing pump power P_{p} manifests itself solely by decrease of the width $\Delta n_{s,r}$ of radial signal-field intensity profile in the crystal output plane (see Fig. 12). Whereas the width $\Delta n_{s,r}$ of radial signal-field intensity profile coincides with the width of pump beam for low-intensity twin beams [20], it is narrower for more intense twin beams. This is explained by more intense amplification of the modes localized close to the pump-beam center relative to those occurring at the tails of the beam. Widths of auto- ($\Delta A_{\mathrm{s},r}$ and $\Delta A_{\mathrm{s},\psi}$) and cross-correlation ($\Delta C_{\mathrm{s},r}$ and $\Delta C_{\mathrm{s},\psi}$) functions as well as their shapes are nearly identical in the crystal output plane, as shown in Fig. 13. Moreover, they do not practically depend on the pump
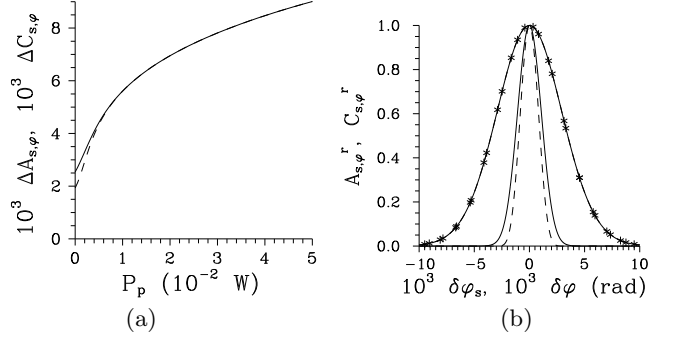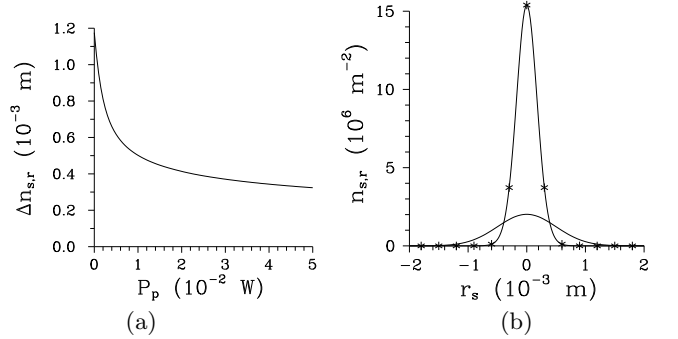
power P_{p}.

Whereas both auto- and cross-correlation functions in the frequency, time and transverse wave-vector domains have compact shapes, long tails and oscillations are characteristic for the correlation functions in the crystal output plane (see Fig. 13) [20]. This stems from a different mode structure found in this case and discussed below. The analysis has shown that the correlation functions $A_{\mathrm{s},r\psi}$ and $C_{\mathrm{s},r\psi}$ are rotationally symmetric and moreless independent on the position inside the emission disc. This originates in the used experimental configuration in which $\Delta C_{\mathrm{s},k}/k_{\mathrm{s}}^{\perp 0} \approx 0.01$. This value is so low that it does not allow to develop variations with the varying position in the crystal output plane. We note that photon pairs emitted at the crystal end contribute to the center of correlation functions, whereas photon pairs generated
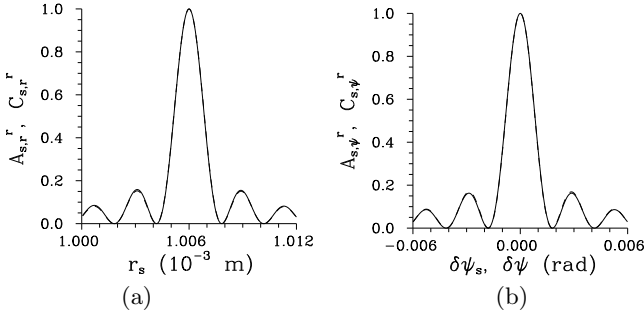
FIG. 13. (a) [(b)] Signal-field intensity auto-correlation function $A_{s,r}^r$ [$A_{s,\psi}^r$] (solid curve) and cross-correlation function $C_{s,r}^r$ [$C_{s,\psi}^r$] (dashed curve) are shown for $P_p = 1 \times 10^{-7}$ W (both curves nearly coincide); $A_{s,r}^r(r_s) \equiv A_{s,r}(r_s, r_s^0)/A_{s,r}(r_s^0, r_s^0)$, $C_{s,r}^r(r_s) \equiv C_{s,r}(r_s, r_i^0)/C_{s,r}(r_s^0, r_i^0)$, $A_{s,\psi}^r(\delta\psi_s) \equiv A_{s,\psi}(\psi_s^0 + \delta\psi_s, \psi_s^0; r_s^0)/A_{s,\psi}(\psi_s^0, \psi_s^0; r_s^0)$, $C_{s,\psi}^r(\delta\psi) \equiv C_{s,\psi}(\psi_s^0 + \delta\psi, \psi_i^0; r_s^0, r_i^0)/C_{s,\psi}(\psi_s^0, \psi_i^0; r_s^0, r_i^0)$; $r_s^0 = r_i^0 = 1.006 \times 10^{-3}$ m; $\psi_s^0 = \psi_i^0$; $w_p = 1 \times 10^{-3}$ m, $\Delta\lambda_p = 1 \times 10^{-10}$ m.

at the beginning of the crystal are observed at the tails of the correlation functions. Thus, the width $\Delta A_{s,r}^a$ of radial signal-field amplitude auto-correlation function is sufficient for the characterization of coherence properties ($\Delta A_{s,r}^a = 2.297 \times 10^{-6}$ m). We note that the width $\Delta A_{s,\psi}^a$ in the azimuthal direction depends on the distance r_s from the disc center. It attains its maximal value ($\Delta A_{s,\psi} = 2\pi$) for $r_s = 0$ m and then monotonously decreases with the increasing distance r_s, in accord with the polar geometry. However, the presence of oscillations in the correlation functions shown in Fig. 13 disqualifies the width $\Delta A_{s,r}^a$ (FWHM) as a suitable quantifier of the extension of field's correlations. Width $\Delta\tilde{A}_{s,r}^a$ determined from the first moments of position and defined in the caption to Fig. 8 has been found suitable in this case. It has also been used in the determination of the number $\tilde{K}_{r\psi}$ of signal-field modes in the crystal output plane plotted in Fig. 8 ($\tilde{K}_{s,r}^a \approx 3.17 K_{s,r}^a$).

The oscillatory behavior of correlation functions and their independence on pump power P_p originate in the form of radial modes $\tilde{u}_{s,ml}(r_s)$ and $\tilde{u}_{i,ml}(r_i)$ given by the transformation from the wave-vector transverse plane based on the Bessel functions [see Eq. (A9) in Appendix A]. There exist two types of modes. Modes obtained for the azimuthal number $m = 0$ have their maximum at $r = 0$ m [see Fig. 14(a)]. They are indispensable for describing the central part of emission disc. On the other hand, modes with $m \neq 0$ have zero intensity for $r = 0$ m and attain their maximal values for $r_{s,max} > 0$ [for $m = 1$, see Fig. 14(b)]. The larger the azimuthal number m, the greater the value of $r_{s,max}$. Fixing the azimuthal number m, all radial modes with different radial numbers l have zeroes in their intensity profiles at the same positions. This property leads to practical independence of the correlation functions on pump power P_p. As the graphs in Fig. 14 indicate, the modes $\tilde{u}_{s,ml}$ with
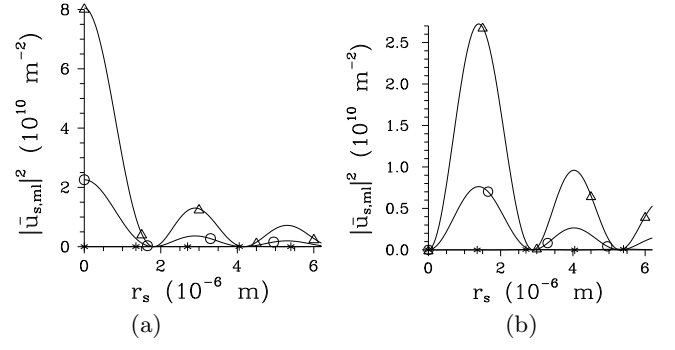

FIG. 14. Intensity profiles $|\tilde{u}_{s,ml}|^2$ of signal-field radial modes in the crystal output plane for $l = 0$ (curve with $\triangle$), 1 ($*$) and 2 ($\circ$) assuming (a) $m = 0$ and (b) $m = 1$. Modes $\tilde{u}_{s,ml}$ are normalized such that $\int_0^\infty dr_s r_s |\tilde{u}_{s,ml}(r_s)|^2 = 1$; $w_p = 1 \times 10^{-3}$ m, $\Delta\lambda_p = 1 \times 10^{-10}$ m.

odd radial numbers l have small intensities compared to those with even radial numbers l. So, the modes with odd numbers l have to be very delocalized in radial direction r and their influence to the properties of twin beams is practically negligible. This behavior has its origin in the shapes of modes $u_{s,ml}$ in the radial wave-vector direction that are close to odd functions in $\delta k^\perp$.

VII. CONCLUSIONS

We have analyzed the properties of general spatio-spectral twin beams in the paraxial and parametric approximations. Considering their spatial and spectral degrees of freedom in their common evolution during the nonlinear interaction, we have investigated the properties of twin beams as they depend on the pump intensity. We have determined auto- and cross-correlation functions of a twin beam in the spectral and temporal domains as well as the transverse wave-vector and crystal output planes in terms of the appropriate paired Schmidt modes. We have mutually compared their behavior. Whereas the spectral and temporal coherence and the coherence in the transverse wave-vector plane increase with the increasing pump intensity, the coherence in the crystal output plane is practically independent on the pump intensity. Whereas the spectral and transverse wave-vector auto-correlation functions are broader than their cross-correlation counterparts for lower pump intensities, the opposed is true for the temporal correlation functions. However, auto- and cross-correlation functions approach each other for higher pump intensities.

Entanglement dimensionality of a twin beam as a function of the pump intensity has been determined and compared with the numbers of modes derived from solely the signal field using either its photon-number statistics or widths of appropriate auto-correlation functions. The numbers of signal-field modes have been confirmed as good quantifiers of entanglement dimensionality of the twin beam.

Practical independence of auto- and cross-correlation functions on the pump intensity in the crystal output plane has been explained by the special structure of paired modes in this plane qualitatively different from the common one occurring, e.g., in the spectral or temporal domains. Moreover, only every second paired mode contributes significantly to the structure of a twin beam for non-collinear geometries.

We believe that this comprehensive analysis of intense twin beams will stimulate further experimental investigations of intense twin beams. Moreover, as all spatio-spectral modes of a twin beam are taken into account, the model allows for its extension to pump intensities at which pump depletion is observed [44, 45].

Appendix A: Properties of twin beams in the transverse wave-vector and crystal output planes

In Appendix A, we define quantities in the transverse wave-vector space determined by spectral averaging as well as quantities in the crystal output plane obtained after temporal averaging. This averaging provides transverse intensity profiles as well as intensity auto- and cross-correlation functions.

The signal-field intensity profile $n_{s,k\varphi}$ in the transverse wave-vector plane is obtained as follows:

$$n_{s,k\varphi}(k_s^{\perp}, \varphi_s) = \langle \hat{a}_s^{\dagger}(k_s^{\perp}, \varphi_s, \omega_s, L)\hat{a}_s(k_s^{\perp}, \varphi_s, \omega_s, L)\rangle_{\|}$$
$$= \sum_q \sum_{ml} |t_{s,ml}(k_s^{\perp}, \varphi_s)|^2 V_{mlq}^2. \quad (A1)$$

In Eq. (A1), symbol $\langle\rangle_{\|}$ means spectral averaging. The radial signal-field intensity profile $n_{s,k}$ is then gives by a cut from the intensity profile $n_{s,k\varphi}$:

$$n_{s,k}(k_s^{\perp}) = n_{s,k\varphi}(k_s^{\perp}, \varphi_s^0 = 0). \quad (A2)$$

Averaged signal-field intensity correlations in the transverse wave-vector plane are described by the following fourth-order auto-correlation function $A_{s,k\varphi}$:

$$A_{s,k\varphi}(k_s^{\perp}, \varphi_s, k_s^{'\perp}, \varphi_s') = \langle \mathcal{N} : \Delta[\hat{a}_s^{\dagger}(k_s^{\perp}, \varphi_s, \omega_s, L)$$
$$\times \hat{a}_s(k_s^{\perp}, \varphi_s, \omega_s, L)]\Delta[\hat{a}_s^{\dagger}(k_s^{'\perp}, \varphi_s', \omega_s', L)$$
$$\times \hat{a}_s(k_s^{'\perp}, \varphi_s', \omega_s', L)] :\rangle_{\|}$$
$$= \sum_q |A_{s,q,k\varphi}^a(k_s^{\perp}, \varphi_s, k_s^{'\perp}, \varphi_s')|^2. \quad (A3)$$

The signal-field amplitude auto-correlation function $A_{s,q,k\varphi}^a$ of mode q is determined as follows:

$$A_{s,q,k\varphi}^a(k_s^{\perp}, \varphi_s, k_s^{'\perp}, \varphi_s')$$
$$= \langle \hat{a}_s^{\dagger}(k_s^{\perp}, \varphi_s, \omega_s, L)\hat{a}_s(k_s^{'\perp}, \varphi_s', \omega_s', L)\rangle_{\|,q}$$
$$= \sum_{ml} t_{s,ml}^*(k_s^{\perp}, \varphi_s)t_{s,ml}(k_s^{'\perp}, \varphi_s')V_{mlq}^2. \quad (A4)$$

Radial ($A_{s,k}$) and azimuthal ($A_{s,\varphi}$) signal-field intensity correlation functions are derived from Eq. (A4) along the relations:

$$A_{s,k}(k_s^{\perp}, k_s^{'\perp}) = A_{s,k\varphi}(k_s^{\perp}, \varphi_s^0 = 0, k_s^{'\perp}, \varphi_s^{'0} = 0),$$
$$A_{s,\varphi}(\varphi_s, \varphi_s') = A_{s,k\varphi}(k_s^{\perp 0}, \varphi_s, k_s^{\perp 0}, \varphi_s'). \quad (A5)$$

Similarly, intensity cross-correlations in the wave-vector signal and idler transverse planes are quantified by the fourth-order correlation function $C_{k\varphi}$:

$$C_{k\varphi}(k_s^{\perp}, \varphi_s, k_i^{\perp}, \varphi_i)$$
$$= \langle \mathcal{N} : \Delta[\hat{a}_s^{\dagger}(k_s^{\perp}, \varphi_s, \omega_s, L)\hat{a}_s(k_s^{\perp}, \varphi_s, \omega_s, L)]$$
$$\times \Delta[\hat{a}_i^{\dagger}(k_i^{\perp}, \varphi_i, \omega_i, L)\hat{a}_i(k_i^{\perp}, \varphi_i, \omega_i, L)] :\rangle_{\|}$$
$$= \sum_q \left| \sum_{ml} t_{s,ml}(k_s^{\perp}, \varphi_s)t_{i,ml}(k_i^{\perp}, \varphi_i)U_{mlq}V_{mlq} \right|^2. \quad (A6)$$

Radial ($C_{s,k}$) and azimuthal ($C_{s,\varphi}$) intensity cross-correlation functions are easily determined from the cross-correlation function $C_{k\varphi}$:

$$C_{s,k}(k_s^{\perp}, k_i^{\perp}) = C_{s,k\varphi}(k_s^{\perp}, \varphi_s^0 = 0, k_i^{\perp}, \varphi_i^0 = \pi),$$
$$C_{s,\varphi}(\varphi_s, \varphi_i) = C_{s,k\varphi}(k_s^{\perp 0}, \varphi_s, k_i^{\perp 0}, \varphi_i). \quad (A7)$$

On the other hand, properties of the twin beams at the crystal output plane (near field) are described by the two-dimensional Fourier transform of eigenmodes t written in Eq. (16) and defined in the transverse wave-vector plane. This transform applied to the radially symmetric geometry leaves us with eigenmodes $\tilde{t}_a$ [$x_a = r_a \cos(\psi_a)$, $y_a = r_a \sin(\psi_a)$],

$$\tilde{t}_{s,ml}(r_s, \psi_s) = \frac{\tilde{u}_{s,ml}(r_s)\exp(im\psi_s)}{\sqrt{2\pi}},$$
$$\tilde{t}_{i,ml}(r_i, \psi_i) = \frac{\tilde{u}_{i,ml}(r_i)\exp(-im\psi_i)}{\sqrt{2\pi}}, \quad (A8)$$

where

$$\tilde{u}_{a,ml}(r_a) = i^m \int_0^{\infty} dk_a^{\perp} \sqrt{k_a^{\perp}} u_{a,ml}(k_a^{\perp})J_m(k_a^{\perp} r_a),$$
$$a = s, i \quad (A9)$$

and J_m stands for the Bessel function of m-th order.

Using eigenmodes $\tilde{t}_{s,ml}$ defined in Eq. (A8), the averaged signal-field photon flux $I_{s,r\varphi}$ in the crystal output plane is expressed as:

$$I_{s,r\psi}(r_s, \psi_s) = 2\epsilon_0 c\langle \hat{E}_s^{(-)}(r_s, \psi_s, L, t_s)\hat{E}_s^{(+)}(r_s, \psi_s, L, t_s')\rangle_{\|}$$
$$= \sum_q \sum_{ml} |\tilde{t}_{s,ml}(r_s, \psi_s)|^2 V_{mlq}^2. \quad (A10)$$

The corresponding radial signal-field intensity profile $I_{s,r}$ is determined as:

$$I_{s,r}(r_s) = I_{s,r\psi}(r_s, \psi_s^0 = 0). \tag{A11}$$

The averaged signal-field intensity auto-correlation function $A_{s,r\psi}$ in the crystal output plane is obtained by the formula analogous to that written in Eq. (A3),

$$
\begin{aligned}
A_{s,r\psi}(r_s, \psi_s, r_s', \psi_s') &= (2\epsilon_0 c)^2 \langle \mathcal{N} : \Delta[\hat{E}_s^{(-)}(r_s, \psi_s, L, t_s) \\
&\times \hat{E}_s^{(+)}(r_s, \psi_s, L, t_s)]\Delta[\hat{E}_s^{(-)}(r_s', \psi_s', L, t_s') \\
&\times \hat{E}_s^{(+)}(r_s', \psi_s', L, t_s')] :\rangle_{\|} \\
&= \sum_q \left| A_{s,q,r\psi}^{a}(r_s, \psi_s, r_s', \psi_s') \right|^2 . \tag{A12}
\end{aligned}
$$

In Eq. (A12), the signal-field amplitude auto-correlation function $A_{s,q,r\psi}^{a}$ characterizing mode q is determined as:

$$
\begin{aligned}
A_{s,q,r\psi}^{a}&(r_s, \psi_s, r_s', \psi_s') \\
&= 2\epsilon_0 c \langle \hat{E}_s^{(-)}(r_s, \psi_s, L, t_s)\hat{E}_s^{(+)}(r_s', \psi_s', L, t_s')\rangle_{\|,q} \\
&= \sum_{ml} \tilde{t}_{s,ml}^*(r_s, \psi_s)\tilde{t}_{s,ml}(r_s', \psi_s')V_{mlq}^2. \tag{A13}
\end{aligned}
$$

The radial ($A_{s,r}$) and azimuthal ($A_{s,\psi}$) signal-field intensity auto-correlation functions are easily derived as follows:

$$
\begin{aligned}
A_{s,r}(r_s, r_s') &= A_{s,r\psi}(r_s, \psi_s^0 = 0, r_s', \psi_s^0 = 0), \\
A_{s,\psi}(\psi_s, \psi_s') &= A_{s,r\psi}(r_s^0, \psi_s, r_s^0, \psi_s'). \tag{A14}
\end{aligned}
$$

Finally, averaged intensity cross-correlations between the signal and idler fields are described by the following fourth-order cross-correlation function:

$$
\begin{aligned}
C_{r\psi}&(r_s, \psi_s, r_i, \psi_i) \\
&= (2\epsilon_0 c)^2 \langle \mathcal{N} : \Delta[\hat{E}_s^{(-)}(r_s, \psi_s, L, t_s)\hat{E}_s^{(+)}(r_s, \psi_s, L, t_s)] \\
&\times \Delta[\hat{E}_i^{(-)}(r_i, \psi_i, L, t_i)\hat{E}_i^{(+)}(r_i, \psi_i, L, t_i)] :\rangle_{\|} \\
&= \sum_q \left| \sum_{ml} \tilde{t}_{s,q}(r_s, \psi_s)\tilde{t}_{i,q}(r_i, \psi_i)U_{mlq}V_{mlq} \right|^2 . \tag{A15}
\end{aligned}
$$

The corresponding radial ($C_{s,r}$) and azimuthal ($C_{s,\psi}$) intensity cross-correlation functions are defined as:

$$
\begin{aligned}
C_{s,r}(r_s, r_i) &= C_{s,r\psi}(r_s, \psi_s^0 = 0, r_i, \psi_i^0 = 0), \\
C_{s,\psi}(\psi_s, \psi_i) &= C_{s,r\psi}(r^0, \psi_s, r^0, \psi_i). \tag{A16}
\end{aligned}
$$

[1] R. W. Boyd, *Nonlinear Optics, 2nd edition* (Academic Press, New York, 2003).
[2] L. Mandel and E. Wolf, *Optical Coherence and Quantum Optics* (Cambridge Univ. Press, Cambridge, 1995).
[3] D. Bouwmeester, A. Ekert, and A. Zeilinger, *The Physics of Quantum Information* (Springer, Berlin, 2000).
[4] S. Carrasco, J. P. Torres, L. Torner, A. V. Sergienko, B. E. A. Saleh, and M. C. Teich, Opt. Lett. **29**, 2429 (2004).
[5] M. I. Kolobov and I. V. Sokolov, Zh. Eksp. Teor. Fiz. **96**, 1945 (1989).
[6] M. I. Kolobov and I. V. Sokolov, Phys. Lett. A **140**, 101 (1989).
[7] O. Jedrkiewicz, Y. K. Jiang, E. Brambilla, A. Gatti, M. Bache, L. A. Lugiato, and P. Di Trapani, Phys. Rev. Lett. **93**, 243601 (2004).
[8] M. Bondani, A. Allevi, G. Zambra, M. G. A. Paris, and A. Andreoni, Phys. Rev. A **76**, 013833 (2007).
[9] J.-L. Blanchet, F. Devaux, L. Furfaro, and E. Lantz, Phys. Rev. Lett. **101**, 233604 (2008).
[10] G. Brida, L. Caspani, A. Gatti, M. Genovese, A. Meda, and I. R. Berchera, Phys. Rev. Lett. **102**, 213602 (2009).
[11] G. Brida, I. P. Degiovanni, M. Genovese, M. L. Rastello, and I. R. Berchera, Opt. Express **18**, 20572 (2010).
[12] V. Boyer, A. M. Marino, R. C. Pooser, and P. D. Lett, Science **321**, 544 (2008).
[13] M. H. Rubin, D. N. Klyshko, Y. H. Shih, and A. V. Sergienko, Phys. Rev. A **50**, 5122 (1994).
[14] J. Peřina Jr., A. V. Sergienko, B. M. Jost, B. E. A. Saleh, and M. C. Teich, Phys. Rev. A **59**, 2359 (1999).
[15] J. Peřina Jr., in *Progress in Optics, Vol. 59*, edited by E. Wolf (Elsevier, Amsterdam, 2014), pp. 89—158.
[16] O. Jedrkiewicz, A. Gatti, E. Brambilla, and P. Di Tra-

pani, Phys. Rev. Lett. **109**, 243901 (2012).
[17] R. Machulka, O. Haderka, J. Peřina Jr, M. Lamperti, A. Allevi, and M. Bondani, Opt. Express **22**, 13374 (2014).
[18] A. Gatti, R. Zambrini, M. San Miguel, and L. A. Lugiato, Phys. Rev. A **68**, 053807 (2003).
[19] E. Brambilla, L. Caspani, L. A. Lugiato, and A. Gatti, Phys. Rev. A **82**, 013835 (2010).
[20] L. Caspani, E. Brambilla, and A. Gatti, Phys. Rev. A **81**, 033808 (2010).
[21] B. Dayan, Y. Bromberg, I. Afek, and Y. Silberberg, Phys. Rev. A **75**, 043804 (2007).
[22] E. Brambilla, A. Gatti, M. Bache, and L. A. Lugiato, Phys. Rev. A **69**, 023802 (2004).
[23] C. K. Law, I. A. Walmsley, and J. H. Eberly, Phys. Rev. Lett. **84**, 5304 (2000).
[24] C. K. Law and J. H. Eberly, Phys. Rev. Lett. **92**, 127903 (2004).
[25] A. Christ, K. Laiho, A. Eckstein, K. N. Cassemiro, and C. Silberhorn, New J. Phys. **13**, 033027 (2011).
[26] A. Avella, M. Gramegna, A. Shurupov, G. Brida, M. Chekhova, and M. Genovese, Phys. Rev. A **89**, 023808 (2014).
[27] J. H. Shapiro and A. Shakeel, J. Opt. Soc. Am. B **14**, 232 (1997).
[28] R. S. Bennink and R. W. Boyd, Phys. Rev. A **66**, 053815 (2002).
[29] I. B. Bobrov, S. S. Straupe, E. V. Kovlakov, and S. P. Kulik, N. J. Phys. **15**, 073016 (2013).
[30] B. Brecht, A. Eckstein, R. Ricken, V. Quiring, H. Suche, L. Sansoni, and C. Silberhorn, Phys. Rev. A **90**, 030302(R) (2014).
[31] M. Annamalai, N. Stelmakh, M. Vasilyev, and P. Kumar,

Opt. Express **19**, 26710 (2011).

[32] W. Wasilewski, A. I. Lvovsky, K. Banaszek, and C. Radzewicz, Phys. Rev. A **73**, 063819 (2006).

[33] A. I. Lvovsky, W. Wasilevski, and K. Banaszek, J. Mod. Opt. **54**, 721 (2007).

[34] A. Christ, B. Brecht, W. Mauerer, and C. Silberhorn, New J. Phys. **15**, 053038 (2013).

[35] P. Sharapova, A. M. Pérez, O. V. Tikhonova, and M. V. Chekhova, Phys. Rev. A **91**, 043816 (2015).

[36] J. Peřina Jr., Phys. Rev. A **87**, 013833 (2013).

[37] M. Stobińska, F. Töppel, P. Sekatski, and M. V. Chekhova, Phys. Rev. A **86**, 022323 (2012).

[38] M. V. Chekhova, G.Leuchs, and M. Zukowski, Opt. Comm. **337**, 27 (2015).

[39] D. S. Hum and M. M. Fejer, Comptes Rendus Physique **8**, 180 (2007).

[40] J. Svozilík and J. Peřina Jr., Phys. Rev. A **80**, 023819 (2009).

[41] P. Kolchin, S. Du, C. Belthangady, G. Y. Yin, and S. E. Harris, Phys. Rev. Lett. **97**, 113602 (2006).

[42] Q. Glorieux, R. Dubessy, S. Guibal, L. Guidoni, J.-P. Likforman, T. Coudreau, and E. Arimondo, Phys. Rev. A **82**, 033819 (2010).

[43] N. V. Corzo, A. M. Marino, K. M. Jones, and P. D. Lett, Phys. Rev. Lett. **109**, 043602 (2012).

[44] A. Allevi and M. Bondani, J. Opt. Soc. Am. B **31**, B14 (2014).

[45] A. Allevi, O. Jedrkiewicz, E. Brambilla, A. Gatti, J. Peřina Jr., O. Haderka, and M. Bondani, Phys. Rev. A **90**, 063812 (2014).

[46] A. Allevi, O. Jedrkiewicz, O. Haderka, J. Peřina Jr., and M. Bondani, in *Proc. of SPIE 9505*, edited by K. Banaszek and C. Silberhorn (SPIE, Bellingham, 2015), p. 95050S.

[47] A. Allevi, M. Lamperti, R. Machulka, O. Jedrkiewicz, E. Brambilla, A. Gatti, J. Peřina Jr., O. Haderka, and M. Bondani, in *Proc. of SPIE 9505*, edited by K. Banaszek and C. Silberhorn (SPIE, Bellingham, 2015), p. 950508.

[48] K. Y. Spasibko, T. S. Iskhakov, and M. V. Chekhova, Opt. Express **20**, 7507 (2012).

[49] A. M. Pérez, T. S. Iskhakov, P. Sharapova, S. Lemieux, O. V. Tikhonova, M. V. Chekhova, and G. Leuchs, Opt. Lett. **39**, 2403 (2014).

[50] J. Peřina, *Quantum Statistics of Linear and Nonlinear Optical Phenomena* (Kluwer, Dordrecht, 1991).

[51] J. Peřina Jr. and J. Peřina, in *Progress in Optics, Vol. 41*, edited by E. Wolf (Elsevier, Amsterdam, 2000), pp. 361—419.

[52] B. Huttner, S. Serulnik, and Y. Ben-Aryeh, Phys. Rev. A **42**, 5594 (1990).

[53] W. Vogel, D. G. Welsch, and S. Walentowicz, *Quantum Optics* (Wiley-VCH, Weinheim, 2001).

[54] M. V. Fedorov, M. A. Efremov, P. A. Volkov, E. V. Moreva, S. S. Straupe, and S. P. Kulik, Phys. Rev. A **77**, 032336 (2008).

[55] M. V. Fedorov, M. A. Efremov, P. A. Volkov, E. V. Moreva, S. S. Straupe, and S. P. Kulik, Phys. Rev. Lett. **99**, 063901 (2007).

[56] J. Peřina Jr., Phys. Scr. p. in print (2015).

[57] M. V. Fedorov and M. I. Miklin, Contemporary Phys. **55**, 94 (2014).

[58] C. Eltschka and J. Siewert, Phys. Rev. Lett. **111**, 100503 (2013).

[59] A. Gatti, T. Corti, E. Brambilla, and D. B. Horoshko, Phys. Rev. A **86**, 053803 (2012).

[60] D. B. Horoshko, G. Patera, A. Gatti, and M. I. Kolobov, Eur. Phys. J. D **66**, 239 (2012).

[61] H. Di Lorenzo Pires, C. H. Monken, and M. P. van Exter, Phys. Rev. A **80**, 022307 (2009).

[62] M. V. Fedorov, M. A. Efremov, A. E. Kazakov, K. W. Chan, C. K. Law, and J. H. Eberly, Phys. Rev. A **72**, 032110 (2005).

[63] K. W. Chan, J. P. Torres, and J. H. Eberly, Phys. Rev. A **75**, 050101(R) (2007).

[64] Y. M. Mikhailova, P. A. Volkov, and M. V. Fedorov, Phys. Rev. A **78**, 062327 (2008).

[65] J. Peřina, *Coherence of Light* (Kluwer, Dordrecht, 1985).

[66] J. Peřina and J. Křepelka, J. Opt. B: Quant. Semiclass. Opt. **7**, 246 (2005).

[67] J. Peřina Jr., O. Haderka, M. Hamar, and V. Michálek, Opt. Lett. **37**, 2475 (2012).

[68] J. Peřina Jr., O. Haderka, V. Michálek, and M. Hamar, Phys. Rev. A **87**, 022108 (2013).

[69] G. Brida, A. Meda, M. Genovese, E. Predazzi, and I. Ruo-Berchera, J. Mod. Opt. **56**, 201 (2009).